UNIVERSITÀ DEGLI STUDI DI MILANO

FACOLTÀ DI SCIENZE E TECNOLOGIE

Corso di Laurea Magistrale in Fisica

A study for the measurement of the Λ baryon electromagnetic dipole moments in LHCb

Relatore: Prof. Nicola NERI

Correlatore: Dott.ssa Elisabetta SPADARO NORELLA

Tesi di Laurea di:
Alessandro DE GENNARO
Matricola 933289
Codice P.A.C.S.: 14.20.-c

Anno Accademico 2020-2021

Introduction

Electric and magnetic dipole moments of particles are sensitive to physics within and beyond the Standard Model. In this thesis, sensitivity studies for the measurement of the Lambda baryon electromagnetic dipole moments based on pseudo experiments will be performed. In addition, the possibility of a first measurement using data collected with the LHCb detector will be explored.

Contents

List of Figures

List of Tables

Chapter 1

Flavour physics and CP symmetry violation

This chapter explores the theoretical framework for the rest of the thesis. Section 1.1 provides a basic introduction to the Standard Model of Particle Physics and flavour physics in particular; Section 1.2 delves into the inner workings of discrete symmetries in quantum physics; Section 1.3 discusses the relevance of electromagnetic dipole moments of elementary particles as a test for CP violation and CPT symmetry; finally, Section 1.4 introduces the main physic motivation for this thesis, the study of dipole moments of the Λ^0 baryon.

1.1 The Standard Model of Particle Physics

Ever since Democritus' philosophy of atomism, one of the driving desires behind mankind's advancements in the fields of natural science has been to reduce reality to its basic components. While one can convincingly argue that we may never fully understand what has come to be known as the quantum world, the Standard Model of Particle Physics (Standard Model, or SM, for short) [1] is as close as physics has to offer to a comprehensive theory of the building blocks of matter and energy.

In addition to predicting a number of then-unknown particles discovered in later years, the Standard Model has shown remarkable consistency against high precision tests, especially in the better known electroweak sector [2]. Despite this, it would be a serious mistake to call it *complete*, even if only for the three fundamental forces it covers. Many experimental evidences, some of which will be discussed in the following pages, have already opened cracks in the model, and many more may emerge in the future; one of the recurring topics of this chapter will thus be the need for physics Beyond the Standard Model (BSM).

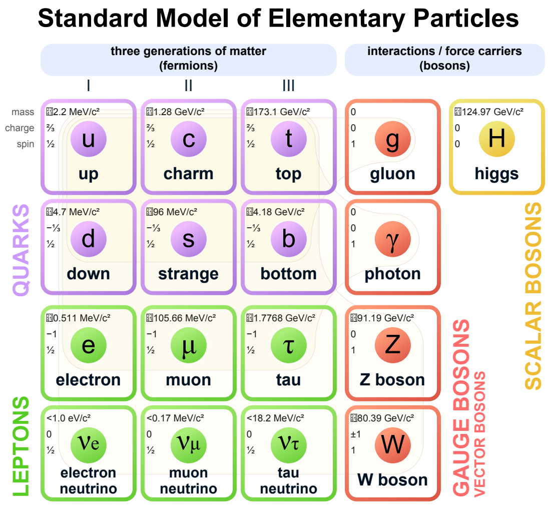

Figure 1.1: The seventeen currently known elementary particles of the Standard Model. Antiparticles are not depicted.

1.1.1 Elementary particles

Intuitively, a particle is said to be *elementary* when no substructure can be probed. A century of efforts in the fields of nuclear, quantum, and high energy physics has whittled down the spectrum of matter to just seventeen unique fundamental particles, colloquially known as the *particle zoo* and depicted in Figure 1.1.

Each particle is joined by an *antimatter particle* (*antiparticle* for short), a companion of opposite charge identified by the prefix *anti-*, e.g. antimuon for the muon; the only exception to this naming convention is the electron, whose antiparticle, for historical reasons, is known as positron. While often omitted for the sake of brevity, antiparticles are elementary particles in every respect, distinct from their partners (bar neutral gauge bosons and the Higgs boson, which are their own antiparticles) and related to them through the transformation of charge conjugation (see Section 1.2.2).

Leptons

Leptons are fermions (half-integer spin particles) not sensitive to the strong nuclear interaction. There are currently six *flavours* of leptons grouped in three generations: each generation comprises a *charged* lepton (electron, muon, tauon) and a *neutral* lepton (electron neutrino, muon neutrino, tauon neutrino).

All charged leptons have a charge of $-e$, where e is defined as the *elemen-*

tary positive charge, and their mass ranges from $\approx 0.5\,\mathrm{MeV}$ for the electron to over $1.7\,\mathrm{GeV}$ for the tauon [3]. By contrast, as the names suggest, all neutrinos are electrically neutral and are assumed massless in the Standard Model[1]; this implies that their only meaningful interactions happen through the weak nuclear force, which grants them their characteristic evasiveness to most particle detectors.

Quarks

Much like leptons, quarks are also fermions existing in three generations. The main difference from the former category is that quarks, besides interacting through weak and electromagnetic forces, are also susceptible to the strong nuclear forces; this allows them to bind together in composite states known as *hadrons*, which are classified as *baryons* (states of three quarks) and *mesons* (states of one quark and one antiquark)[2].

Quarks can be classified as *up-type* (up, charm and top quarks) and *down-type* (down, strange and bottom quarks): up-type quarks have a fractionary charge of $+\frac{2}{3}e$, whereas down-type quarks have a charge of $-\frac{1}{3}e$. All quarks also have one of three *color* charges (red, green or blue), while antiquarks similarly have one of three *anti-color* charges (antired, antigreen or antiblue). A combination of all three colors/anti-colors or a combination of a color and its matching anticolor produces *colorless* particles, a property of all observed quark composite states.

Unlike leptons, quarks are impossible to observe directly: according to the phenomenon of *color confinement*, the energy of the interaction field between two color charges being pulled apart increases with their distance until it becomes high enough to create a quark-antiquark pair. This process of *fragmentation* develops many times over in such a way that the final observable state is entirely composed of colorless particles. For this reason, high energy physics experiments such as LHCb do not detect free quarks, instead observing cone-shaped streams of hadrons known as *hadronic jets*.

Gauge bosons and fundamental interactions

In quantum field theory, the interaction between two fields is implemented through the exchange of an intermediary particle known as *force carrier*. In the Standard Model all force carriers are vector (spin 1) bosons known as *gauge bosons*. The name is owed to the *gauge principle* used to introduce them: the

[1] The observation of flavour oscillation in solar neutrinos shows that neutrinos do in fact have non-zero, albeit very small, mass [4].

[2] As recently as 2003, evidence has surfaced for the existence of exotic hadrons composed of four (*tetraquarks*) [5] and five quarks (*pentaquarks*) [6].

localization of a global continuous symmetry group provides the free fermion Lagrangians with interaction terms with the proviso that one or more bosonic fields are introduced.

The gauge principle accounts for the implementation of three fundamental interactions along with their gauge bosons: the *strong nuclear force* with its massless gluon, responsible for the binding of both quarks inside baryons and nucleons inside atomic nuclei; the *electromagnetic force* mediated by the massless photon, the importance of which should be known from everyday life; and the *weak nuclear force* with two massive $W^{\pm}$ and Z bosons, the source of many subnuclear processes such as β radioactivity.

The latter two forces share a unified description in the Glashow-Weinberg-Salam theory as a single *electroweak interaction* and are introduced via localization of a $\mathrm{SU}(2)_L \otimes \mathrm{U}(1)_Y$ symmetry group, the first related to the conservation of weak isospin in left-handed chirality states and the second to the conservation of hypercharge. Quantum chromodynamics (QCD), the theory of the strong nuclear force, is based on a separate $\mathrm{SU}(3)_C$ symmetry acting on the three-dimensional space of color charges.

There are no gauge bosons nor gauge theories associated to the fourth known fundamental force, gravity. Since every attempt to reconcile the general theory of relativity with quantum mechanics has failed so far, gravity is presently excluded from the Standard Model; this doesn't affect SM predictions at the subatomic level on account of the remarkably low intensity of said force, over 30 orders of magnitude lower than the weak interaction.

The Higgs boson

The Higgs boson is one of the latest additions to the Standard Model, being proposed in 1964 [7] and observed in 2012 by the ATLAS [8] and CMS [9] collaborations. Its introduction solved perhaps the most insidious SM shortcoming at the time: gauge theories, which the model was built on, only worked under the assumption that all particles involved were massless, whereas the local invariance would fall apart (*gauge breaking*) when adding a free mass term.

By contrast, the Higgs field accounts for mass generation of the weak bosons $W^{\pm}$ and Z via the Brout-Englert-Higgs mechanism resulting from the spontaneous electroweak symmetry breaking; elementary fermions also gain mass through a distinct, Yukawa-like interaction with the field.

1.1.2 Flavour physics

A reader unfamiliar with SM terminology may find amusing the use of the word *flavour* to refer to what have been so far presented as different kinds of particles altogether. However quirky, the lexical choice highlights a defining feature: flavour, much like the degree of sweetness in a recipe, can change [10].

As often happens in particle physics, the rules are somewhat easier for leptons. For a given generation $\ell = (e, \mu, \tau)$, one can define a *lepton family number* L_ℓ as the difference between the number of particles and antiparticles of said generation, charged leptons and neutrinos alike:

$$L_\ell \coloneqq n(\ell^-) - n(\ell^+) + n(\nu_\ell) - n(\bar{\nu}_\ell). \tag{1.1}$$

For all three generations, L_ℓ is conserved in every interaction except neutrino oscillations.

Quarks are not as straightforward. A similarly defined quark flavour number, such as the so-called *topness* (or *truth*)

$$T \coloneqq n(t) - n(\bar{t}), \tag{1.2}$$

is preserved through EM and strong interactions, but can change when the state undergoes a *weak charged interaction*, i.e. a weak interaction mediated by the charged gauge bosons $W^\pm$. In fact, one finds that weak interactions for quarks can be accurately described if we assume that the weak eigenstates (d', s', b') of down-type quarks, i.e. the weak isospin doublet partners to up-type quarks, are related to the free mass eigenstates (d, s, b) through a rotation:

$$\begin{pmatrix} d' \\ s' \\ b' \end{pmatrix} = \begin{pmatrix} V_{ud} & V_{us} & V_{ub} \\ V_{cd} & V_{cs} & V_{cb} \\ V_{td} & V_{ts} & V_{tb} \end{pmatrix} \begin{pmatrix} d \\ s \\ b \end{pmatrix}. \tag{1.3}$$

In this notation, the probability for a quark of flavour i to change into a quark of flavour j as a result of a weak charged interaction is proportional to $|V_{ij}|^2$.

The unitary rotation matrix is known as the Cabibbo-Kobayashi-Maskawa (CKM) matrix V_{CKM}. The moduli of its components up to the third decimal place, according to the most recent estimates [3], are

$$\begin{pmatrix} |V_{ud}| & |V_{us}| & |V_{ub}| \\ |V_{cd}| & |V_{cs}| & |V_{cb}| \\ |V_{td}| & |V_{ts}| & |V_{tb}| \end{pmatrix} \approx \begin{pmatrix} 0.974 & 0.224 & 0.004 \\ 0.221 & 0.987 & 0.041 \\ 0.008 & 0.039 & 1.013 \end{pmatrix}. \tag{1.4}$$

A full definition of the CKM matrix requires four independent parameters. Particularly useful for the following sections is the standard parameterization with three angles θ_{12}, θ_{23}, θ_{13}, expressing the mixing between different quark generations, and a complex phase δ_{13}. Defining $s_{ik} \coloneqq \sin\theta_{ik}$ and $c_{ik} \coloneqq \cos\theta_{ik}$, V_{CKM} can be written as

$$V_{\text{CKM}} = \begin{pmatrix} c_{12}c_{13} & s_{12}c_{13} & s_{13}e^{-i\delta_{13}} \\ -s_{12}c_{23} - c_{12}s_{23}s_{13}e^{i\delta_{13}} & c_{12}c_{23} - s_{12}s_{23}s_{13}e^{i\delta_{13}} & s_{23}c_{13} \\ s_{12}s_{23} - c_{12}c_{23}s_{13}e^{i\delta_{13}} & -c_{12}s_{23} - s_{12}c_{23}s_{13}e^{i\delta_{13}} & c_{23}c_{13} \end{pmatrix} \tag{1.5}$$

The phase δ_{13} is known as the CP-violating phase. To fully understand what it means and its role in particle physics, however, a digression into discrete symmetries is needed.

1.2 Discrete symmetries and CP violation

In quantum mechanics, a system described by a Hamiltonian $\hat{\mathcal{H}}$ is *symmetric* under a transformation $\hat{S}$ if the two operators commute, i.e.

$$\left[\hat{\mathcal{H}}, \hat{S}\right] = 0. \tag{1.6}$$

Symmetries are of great relevance in physics on account of Noether's theorem, which establishes a relationship between the *continuous* symmetry of a system and a corresponding conservation law; the emphasis is on the requirement of continuity, meaning the related transformation changes the system «in a smooth way», much like a rotation does. An example of this principle has already been presented earlier in this thesis: the three symmetry groups employed in SM gauge theories all imply the conservation of a specific charge, be it weak isospin, hypercharge, or color.

By contrast, this section will delve into *discrete* symmetries [11], which do not share said «smoothness» property. The absence of a Noether-like theorem for this class of transformations does not detract from their importance in physics: as will be shown, the three symmetries we'll focus on have a remarkable influence on many fields of study.

1.2.1 Parity inversion

By definition, the *parity inversion* (or simply *parity*) transformation $\hat{P}$ flips the sign of the three spatial coordinates:

$$\hat{P} : \begin{pmatrix} x \\ y \\ z \end{pmatrix} \to \begin{pmatrix} -x \\ -y \\ -z \end{pmatrix}. \tag{1.7}$$

Its action on a quantum $|\psi(\vec{x}, t)\rangle$ is therefore

$$\hat{P}\,|\psi(\vec{x}, t)\rangle = |\psi(-\vec{x}, t)\rangle\,. \tag{1.8}$$

More interestingly, for parity eigenstates (known as *parity-defined* states) a parity quantum number can be introduced; such states may have a *P-parity* eigenvalue $\eta_P = +1$ (parity-even states) or $\eta_P = -1$ (parity-odd states). Since by definition $\hat{P}^2 = \mathbb{1}$, where $\mathbb{1}$ is the identity operator, these are the only two allowed P-parity values.

A similarly dichotomous behaviour is observed on both scalar and vector quantities commonly used in classical physics, such as momenta and electromagnetic fields. Parity-even scalar quantities are called *true scalars* or just *scalars* (e.g. energy), whereas parity-odd ones are called *pseudoscalars* (e.g. helicity). The same distinction is present for vector quantities, which are either *polar vectors* (e.g. angular momentum) or *axial vectors* (e.g. linear momentum).

As far as is currently known, gravity, electromagnetic and strong nuclear interactions conserve parity. The same cannot be said for the weak interaction, the P-violating properties of which were first proven in the 1956 Wu experiment on the ^{60}Co β^- decay [12].

1.2.2 Charge conjugation

The transformation of *charge conjugation* $\hat{C}$ changes the sign of all electric charges:

$$\hat{C} : q \to -q. \tag{1.9}$$

It should be readily apparent that $\hat{C}$ has close ties with the concept of antimatter. In fact, the action of charge conjugation turns a quantum state into its antimatter partner, inverting the sign of all flavour quantum numbers in the process:

$$\hat{C} \left|\psi\right\rangle = \left|\bar{\psi}\right\rangle . \tag{1.10}$$

For single-particle systems, the only possible $\hat{C}$ eigenstates are particles that are their own antiparticle, like the photon, for which a C-parity $\eta_C = \pm 1$ is defined by analogy with the P-parity eigenvalue.

Unlike in the case of parity, there isn't a single breakthrough experiment credited for showing that the weak interaction is not C-symmetric: it was known from theory that parity violation in a weak process, when observed under certain conditions, would also imply a violation of charge conjugation, with such a violation being confirmed shortly after Wu's results [13]. As for the other three fundamental interactions, no evidence of C symmetry violation has surfaced so far.

1.2.3 Time reversal

Perhaps the most intuitively named of the three discrete symmetries discussed here, *time reversal* $\hat{T}$ does exactly what it promises:

$$\hat{T} : t \to -t. \tag{1.11}$$

The action of time reversal on a quantum state is represented by an *antiunitary* (unitary and antilinear) operator, which implies a complex conjugation on top of the time reversal itself:

$$\hat{T} \left| \psi(\vec{x}, t) \right\rangle = \left| \psi^*(\vec{x}, -t) \right\rangle \tag{1.12}$$

There are a number of arguments for the antiunitarity of $\hat{T}$, the most straightforward being that it prevents final states with negative energy.

Once more, gravity, strong and electromagnetic forces are T-symmetric, whereas the weak nuclear force isn't. However, as will be explained shortly, this knowledge isn't the result of a direct experiment, instead exploiting a side effect of the CPT theorem.

1.2.4 CP symmetry and violation

The sequential combination of C, P and T transformations, commonly designated as CPT symmetry, plays a key role in the foundations of quantum physics. As well as being the only combination of said transformations still observed to be a symmetry of physical laws, the *CPT theorem* states that any Lorentz-invariant local quantum field theory must be CPT-symmetric. Because a violation of the CPT symmetry would imply the collapse of the modern quantum physics framework, it is generally accepted that a T-violating process must also be a CP-violating process. This bears an important consequence on the study of discrete symmetry violations: because of the self-evident hindrances in building a time-reversed experimental setup outside of trivial cases, every test of T violation becomes by necessity a test of CP violation.

Setting this notion aside, CP symmetry is an interesting field of study in and of itself [14]. For one thing, while C and P symmetries are maximally violated by the weak interaction, CP isn't; this is readily seen with the chirally left-handed neutrino, which possesses a CP-partner (the right-handed antineutrino) despite lacking both a P-partner (the right-handed neutrino) and a C-partner (the left-handed antineutrino). The subject of CP violation is also closely tied to another long-standing dilemma in both particle physics and cosmology: the observed asymmetry between matter and antimatter in our Universe. A perfectly CP-symmetric system would produce a roughly equal number of particles and antiparticles, which would annihilate one another and yield an empty Universe; our very existence implies a primordial imbalance that resulted in baryogenesis and therefore some degree of CP violation.

Since gravity, EM and strong interactions all individually conserve parity and charge conjugation, it stands to reason that they are also CP-symmetric, leaving the weak nuclear interaction as the only possible CP-violating fundamental force. Experiments conducted over the last 50 years have found that, despite CP still being preserved in most weak processes, some select interactions show evidence of CP violation.

The first indirect discovery came in 1964 by Christenson et al. [15], who observed the long-lived neutral kaon two-pion decay $K_L^0 \to \pi^+\pi^-$ with a branching ratio of $\approx 10^{-3}$ over all charged modes. This result could only be explained by assuming that the K_L^0 weak eigenstate is a mixture of both $\eta_{CP} = \pm 1$ eigenstates, with the ability to oscillate between the two. A more direct evidence was found in 1999 by the KTeV collaboration at Fermilab [16] via the observation of differing decay rates in $K_{L/S}^0 \to \pi^+\pi^-$ against $K_{L/S}^0 \to \pi^0\pi^0$ channels, and CP violation in weak processes was definitely established in the early 2000s via studies on B mesons decays conducted in so-called «B-factories» such as BaBar at SLAC [17] and Belle at KEK [18].

Despite the significant number of experimental evidences collected ever since, the extent of known CP-violating processes is several orders of magnitude below what is expected from cosmological estimates. The matter-antimatter imbalance at the time when the Universe cooled below the pair production threshold temperature can be quantified through the *baryon asymmetry parameter* [19], computed as the difference between the densities of baryons and antibaryons divided by their sum:

$$\eta \coloneqq \frac{n_B - n_{\bar{B}}}{n_B + n_{\bar{B}}}. \tag{1.13}$$

While this parameter cannot be directly measured at the present time, we can approximate it by noting that almost no antimatter currently exists in the Universe ($n_{\bar{B}} \approx 0$) and almost all of the original matter will have annihilated into photons ($n_B + n_{\bar{B}} \approx n_\gamma$):

$$\eta \approx \frac{n_B}{n_\gamma}. \tag{1.14}$$

Both of these quantities can be probed by studying the intergalactic medium and the cosmic microwave background, finding $\eta_{\text{obs}} \approx 10^{-10}$ [20]. As for the Standard Model prediction, all SM sources of CP violation arise from quark mixing, and more specifically from the δ_{13} complex phase mentioned in the parameterization (1.5) of the CKM matrix. Computing the baryon asymmetry parameter with this knowledge leads to a much lower $\eta_{\text{SM}} \approx 10^{-20}$ [19].

New sources of CP violation are therefore required to match the observed value, with a promising field being the search for intrinsic electromagnetic dipole moments [14].

1.3 Electromagnetic dipole moments

1.3.1 EDMs

The electric dipole moment (EDM) $\vec{\delta}$ is the measure of a system's *polarity*, i.e. the spatial separation of positive and negative charges within the system. For the simplest of the relevant charge configurations, a dipole of point charges $\pm q$ separated by a distance r, the EDM is expressed as

$$\vec{\delta} = q\vec{r}, \tag{1.15}$$

where the displacement vector $\vec{r}$ points from the negative charge to the positive one.

It's hardly a feat of imagination to theorize that a composite particle like the neutron could acquire an EDM, even if the three quarks inside it cannot be thought of as a system of charges in the classical sense. It may be less intuitive that elementary, point-like particles such as electrons and quarks could also gain one, due to quantum effects resulting in the creation and destruction of virtual particles (so-called *loops* in higher order Feynman diagrams).

For a spin-$\frac{1}{2}$ particle, its EDM is written in Gaussian units as [21]

$$\vec{\delta} = d\frac{\mu_B}{2}\vec{s}, \tag{1.16}$$

where d is a dimensionless quantity referred to as *gyroelectric factor*,

$$\mu_B = \frac{e\hbar}{2mc}, \tag{1.17}$$

is the particle magneton, c is the speed of light in a vacuum, m is the particle mass and

$$\vec{s} = 2\frac{\langle\vec{S}\rangle}{\hbar} \tag{1.18}$$

is the spin polarization vector, related to the average value of the spin $\vec{S}$ divided by the reduced Planck constant $\hbar$.

When the particle crosses an external electric field $\vec{E}$, its EDM will polarize by changing the direction of the spin. This introduces an energy term in the system's Hamiltonian with the form

$$H_{\text{EDM}} = -\vec{\delta}\cdot\vec{E}. \tag{1.19}$$

One can now check how the term (1.19) behaves when acted upon by some of the discrete transformations outlined in Section 1.2. The behaviour of spin $\vec{S}$, and therefore of the spin-related EDM $\vec{\delta}$, can easily be shown to be that of polar vectors, i.e. parity-even. By contrast, the electric field $\vec{E}$ is an axial vector, i.e. parity-odd, which makes H_{EDM} a parity-odd pseudoscalar:

$$H_{\mathrm{EDM}} \xrightarrow{\hat{P}} -H_{\mathrm{EDM}}. \tag{1.20}$$

When considering time reversal $\hat{T}$, the situation is specular: the EDM $\vec{\delta}$ flips its sign, whereas the electric field $\vec{E}$ remains unchanged, implying

$$H_{\mathrm{EDM}} \xrightarrow{\hat{T}} -H_{\mathrm{EDM}}. \tag{1.21}$$

The above result in particular contains a crucial piece of information: assuming the validity of the CPT theorem, a Hamiltonian containing the EDM's interaction term (1.19) can only be CP-symmetric if the average (or *permanent*) EDM of the particle is zero.

It follows that, for a particle to have a permanent EDM, CP symmetry must be violated in some measure[3]. As explained in Section 1.2.4, the only known source of CP violation within the Standard Model is the complex phase δ_{13} in quark mixing, which may give a small contribution to the EDMs of point-like particles such as electrons ($\delta \lesssim 10^{-40}\, e\,\mathrm{cm}$ [22]) and quarks ($\delta \lesssim 10^{-34}\, e\,\mathrm{cm}$ [23]) via beyond-tree-level diagrams. Composite particles such as baryons are accorded some leeway on account of their finite size: the weak interaction between quarks inside the neutron, for instance, contributes to a possible EDM up to $\delta \lesssim 10^{-31}\, e\,\mathrm{cm}$ [24].

In all cases, the predicted SM contributions are orders of magnitudes below the sensitivity reached by current generation experiments. For all intents and purposes, the observation of a non-zero permanent EDM in a baryon would imply the discovery of a BSM source of CP violation.

1.3.2 MDMs

The magnetic dipole moment (MDM) $\vec{\mu}$ of a system can be interpreted as the measure of how intense a torque the system experiences when crossing a magnetic field $\vec{B}$:

$$\vec{\tau} = \vec{\mu} \times \vec{B}. \tag{1.22}$$

[3]This line of reasoning only applies to systems that are parity eigenstates. Water molecules are notoriously polar, but their EDMs do not violate any fundamental symmetry because the molecule's ground state is a superposition of parity-even and parity-odd eigenstates.

Unlike the case of EDMs, the extension of MDMs from classical to quantum physics is less extreme, as long as one acknowledges the affinity between angular momentum and a particle's intrinsic spin. A classical rotating body with charge q, mass m and angular momentum $\vec{L}$ gains an MDM in the form

$$\vec{\mu} = \frac{q}{2m}\vec{L}, \tag{1.23}$$

assuming charge and mass are identically distributed. A very similar relation holds for a non-classical, point-like spin-$\frac{1}{2}$ particle [21]:

$$\vec{\mu} = g\frac{\mu_B}{2}\vec{s} \tag{1.24}$$

Here g is the dimensionless *gyromagnetic factor* accounting for the transition from classical to quantum physics, whereas μ_B and $\vec{s}$ are the same particle magneton and spin polarization vector defined in equations (1.17) and (1.18) respectively.

Similary to EDMs, MDMs also induce a spin rotation when subjected to a magnetic field $\vec{B}$, introducing a Hamiltonian term

$$H_{\mathrm{MDM}} = -\vec{\mu}\cdot\vec{B}. \tag{1.25}$$

Under parity and time reversal transformations, the MDM $\vec{\mu}$ behaves in the same way as the EDM $\vec{\delta}$, both being dependent on the particle's spin $\vec{S}$ (odd under $\hat{P}$, even under $\hat{T}$). In contrast with $\vec{E}$, however, the magnetic field $\vec{B}$ behaves in the *same* way as $\vec{\mu}$, effectively cancelling out their signs when the Hamiltonian (1.25) is acted upon:

$$H_{\mathrm{MDM}} \xrightarrow{\hat{P}} H_{\mathrm{MDM}}, \tag{1.26}$$

$$H_{\mathrm{MDM}} \xrightarrow{\hat{T}} H_{\mathrm{MDM}}. \tag{1.27}$$

Factoring in the CPT theorem, this result entails that a non-zero intrinsic MDM for fundamental particles does not imply CP violation. For this reason, measurements of MDMs are instead used as *precision tests* of the CPT theorem, since their values should not change between a particle and its antimatter partner.

1.3.3 Measurement of EDMs and MDMs

For the purposes of this thesis, the measurement of EDMs and MDMs of a particle is performed by exploiting the precession of spin in an electromagnetic field [25]. In the laboratory frame, a neutral particle flying with velocity $\vec{\beta}$

through homogeneous electromagnetic fields $\vec{E}$ and $\vec{B}$ experiences a precession of the non-relativistic spin polarization vector $\vec{s}$ described by the equation

$$\frac{d\vec{s}}{dt} = \vec{s} \times \vec{\Omega}, \qquad \vec{\Omega} := \vec{\Omega}_{\mathrm{EDM}} + \vec{\Omega}_{\mathrm{MDM}}. \tag{1.28}$$

The angular velocity vector $\vec{\Omega}$ is itself the sum of two contributions due to the respective intrinsic dipole moments of the particle:

$$\vec{\Omega}_{\mathrm{EDM}} = \frac{d\mu_B}{\hbar}\left(\vec{E} - \frac{\gamma}{\gamma+1}(\vec{\beta}\cdot\vec{E})\vec{\beta} + \vec{\beta}\times\vec{B})\right), \tag{1.29}$$

$$\vec{\Omega}_{\mathrm{MDM}} = \frac{g\mu_B}{\hbar}\left(\vec{B} - \frac{\gamma}{\gamma+1}(\vec{\beta}\cdot\vec{B})\vec{\beta} - \vec{\beta}\times\vec{E})\right). \tag{1.30}$$

Assuming $\vec{E} = 0$, as will be the case in the experimental setup employed in this work, the angular velocity simplifies to

$$\vec{\Omega} = \frac{\mu_B}{\hbar}\left[d\vec{\beta}\times\vec{B} + g\left(\vec{B} - \frac{\gamma}{\gamma+1}(\vec{\beta}\cdot\vec{B})\vec{\beta}\right)\right]. \tag{1.31}$$

An analytical solution of the above system of equations is possible under the approximation that the precession of the particle spin depends only on the integrated value of the magnetic field $\vec{B}$ along the particle's flight path l. In the absence of field gradients, dictated by the homogeneity requirement, such integrated field $\vec{D}$ can be written as

$$\vec{D} := \int_0^l dl'\vec{B}(\vec{r}_0 + \hat{\beta}l') \approx \langle\vec{B}\rangle\, l, \tag{1.32}$$

where $\hat{\beta}$ is the normalized vector of $\vec{\beta}$. Defining $\hat{\Omega}$ in the same way, the time evolution of the spin polarization vector $\vec{s}$ ($\vec{s}(0) = \vec{s}_0$) is

$$\vec{s}\,(l) = \left(\vec{s}_0\cdot\hat{\Omega}\right)\hat{\Omega} + \left[\vec{s}_0 - \left(\vec{s}_0\cdot\hat{\Omega}\right)\hat{\Omega}\right]\cos\left(\left|\vec{\Omega}\right|t\right) + \left(\vec{s}_0\times\hat{\Omega}\right)\sin\left(\left|\vec{\Omega}\right|t\right). \tag{1.33}$$

From an experimental point of view, measurement of time isn't trivial; instead, one can efficiently measure the flight length of an unstable particle $l = \beta ct$ during its lifetime. The equation describing the spin precession as a function of l has a very similar form to (1.33):

$$\vec{s}\,(l) = \left(\vec{s}_0\cdot\hat{\Phi}\right)\hat{\Phi} + \left[\vec{s}_0 - \left(\vec{s}_0\cdot\hat{\Phi}\right)\hat{\Phi}\right]\cos\left|\vec{\Phi}\right| + \left(\vec{s}_0\times\hat{\Phi}\right)\sin\left|\vec{\Phi}\right|, \tag{1.34}$$

with

$$\vec{\Phi} = \frac{\mu_B}{|\vec{\beta}|\hbar c}\left[d\vec{\beta}\times\vec{D} + g\left(\vec{D} - \frac{\gamma}{\gamma+1}(\vec{\beta}\cdot\vec{D})\vec{\beta}\right)\right] \tag{1.35}$$

and $\vec{D}$ defined as in (1.32).

Equation (1.34) therefore provides a way to measure the values of EDMs and MDMs for neutral particles by studying the change in polarization after their flight through a magnetic field. For unstable particles, the polarization at the time of decay can be inferred in a fairly straightforward way from the angular distribution of their products. Conversely, theoretical knowledge or measurement of the original spin polarization $\vec{s}_0$ of the particle are both far from easy tasks in a general setting. Thankfully, in certain instances such as the one covered in this thesis, $\vec{s}_0$ can be known by exploiting the same parity violation of weak interactions discovered in 1956 by Wu and her collaborators.

1.4 Proposal of a measurement of the Λ^0 electromagnetic dipole moments with the LHCb detector

The Λ^0 baryon, also historically known as the Λ^0 hyperon[4] and sometimes labelled only as Λ, is a spin-$\frac{1}{2}$ baryon with (u, d, s) valence quarks. As the first identified baryon beyond the two nucleons, it played a key role in the discovery and christening of the strange quark: its mass of $\approx 1116\,\mathrm{MeV}/c$ [3], the lightest among s-bearing baryons, meant its only viable decay channels were mediated by the flavour-changing weak interaction, giving the Λ^0 a much longer half-life than expected; this property was dubbed *strangeness*, a name later inherited by the new quark that indirectly caused it.

The Λ^0 baryon is also a prime candidate to probe CP violation. Unlike in the case of the prospective discovery of a neutron EDM[5], a non-zero Λ^0 baryon EDM could not be explained by any phenomena within the Standard Model and would therefore imply the existence of BSM physics.

1.4.1 Previous measurements of the Λ^0 dipole moments

[Misure precedenti.]

[4] A *hyperon* is a baryon with one or more strange quarks, but no heavier quarks. The nomenclature emerged in the period following the discovery of the strange quark, when no further quarks besides the first three were known; nowadays, the term is rarely used.

[5] Quantum chromodynamics allows for a CP-violating term proportional to the QCD vacuum angle θ. Current measurements of the neutron EDM [26] constrain $\theta \lesssim 10^{-10}$, a fine-tuning suppression known as the *strong CP problem*; nevertheless, experimental discovery of a non-zero neutron EDM could be traced back to this term and would not necessarily require the introduction of new physics.

1.4.2 Proposal overview

My work in this thesis aims to exploit the spin precession technique outlined in Section 1.3.3 to perform a measurement of the Λ^0 baryon electromagnetic dipole moments with the LHCb detector at the Large Hadron Collider (see Chapter 2). Specifically, the unique features of the LHCb experimental setup and a careful selection of the Λ^0 production channel will allow for significant simplifications of the general equation (1.34) for neutral unstable particles.

The LHCb detector is equipped with a suitable [quanti tesla] magnetic field directed along the laboratory frame y axis. Gradient field effects for the $\vec{B}$ field within the detector acceptance are negligible, being estimated at [25]

$$\frac{\hbar}{2mc}\frac{\beta\gamma}{\gamma+1}\frac{|\nabla B|}{B} \approx 7.4 \times 10^{-16}, \tag{1.36}$$

with $B := |\vec{B}|$. The Λ^0 baryon's average mean life of $\approx 2.6 \times 10^{-10}\,\mathrm{s}$ [3] allows a sizeable number of them to traverse the full LHCb magnetic field region [regione in z] before decaying, making it possible to measure both the initial and final polarizations to infer spin precession.

1.4.3 Polarization measurements

The problem concerning the measurement of the Λ^0 initial polarization is circumvented by selecting Λ^0 produced through the weak decay of the bottom baryon Λ_b^0

$$\Lambda_b^0 \to J/\psi\,(\to \mu^+\mu^-)\,\Lambda^0\,(\to p\pi^-), \tag{1.37}$$

as well as its charge-conjugate[6]

$$\bar{\Lambda}_b^0 \to J/\psi\,(\to \mu^+\mu^-)\,\bar{\Lambda}^0\,(\to \bar{p}\pi^+). \tag{1.38}$$

Parity violation in this decay produces Λ^0 with almost 100% longitudinal polarization [27], meaning that the original polarization can be computed from the Λ^0 reconstructed momentum.

The nature of LHCb as a forward detector implies that Λ^0 baryons will mostly fly along the laboratory frame z axis, and therefore the initial polarization can be written as $\vec{s_0} = (0, 0, s_0)$. Equation (1.34) for the Λ^0 spin precession after the magnetic field region can thus be simplified assuming a field $\vec{B} = (0, B_y, 0)$:

$$\vec{s} = \begin{cases} s_x = -s_0 \sin\Phi \\ s_y = -s_0 \frac{d\beta}{g} \sin\Phi \\ s_z = s_0 \cos\Phi \end{cases}, \tag{1.39}$$

[6] For the sake of brevity, charge-conjugate notation will be omitted in the rest of this thesis except where relevant to the topic at hand.

with

$$\Phi = \frac{D_y \mu_B}{\beta \hbar c} \sqrt{d^2 \beta^2 + g^2} \approx \frac{g D_y \mu_B}{\beta \hbar c}, \tag{1.40}$$

$\beta \coloneqq \left|\vec{\beta}\right|$ and

$$D_y \coloneqq D_y(l) = \int_0^l dl' B_y. \tag{1.41}$$

Note from equation (1.39) that a non-vanishing intrinsic EDM introduces a s_y component to the final polarization, the MDM precession of which would otherwise be confined to the xz plane.

The polarization *after* the magnetic field can be probed by studying the angular distribution of the $\Lambda^0 \to p\pi^-$ decay products. It can be shown (see Appendix A) that the expected angular distribution for said decay is

$$\frac{dN}{d\Omega'} = 1 + \alpha \vec{s} \cdot \hat{k}, \tag{1.42}$$

where $\Omega' \coloneqq (\theta', \phi')$ is the solid angle in the Λ^0 helicity frame (see Figure 1.2) corresponding to the momentum direction of the proton, pointing in the direction of the unit vector

$$\hat{k} = \begin{pmatrix} \sin\theta' \cos\phi' \\ \sin\theta' \sin\phi' \\ \cos\theta' \end{pmatrix}, \tag{1.43}$$

and $\alpha \approx 0.732$ [3] is the decay asymmetry parameter. The combined measurements of the initial polarization (from the momenta of Λ^0 produced via decays (1.37) and (1.38)) and the final polarization (from angular distribution (1.42)) allow for a study of both Λ^0 dipole moments based on the single components of the precession (1.39).

Deviations from this simplified treatment ought to be considered when taking into account the different relevant frames of reference, three of which are sketched in Figure 1.2:

- the laboratory frame S_L, with the z axis along the proton beam and the y axis along the vertical coordinate;

- the heavy baryon Λ_b^0 helicity frame S_H, with the z axis given by the Λ_b^0 momentum in S_L and the x axis parallel to the normal to its production plane;

- the two Λ^0 helicity frames S_Λ and $S_{\Lambda\mathrm{L}}$. These are functionally the same frame of reference, the key difference being that the z axis is defined in the direction of the Λ^0 momentum in S_H and S_L respectively.

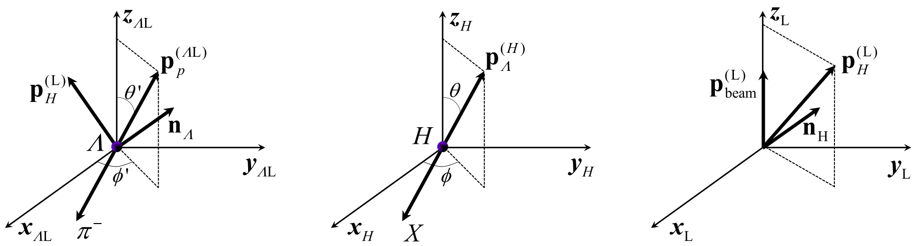

Figure 1.2: Frames of reference for the $\Lambda_b^0 \to J/\psi\,(\to \mu^+\mu^-)\,\Lambda^0\,(\to p\pi^-)$ decay: on the *left* the Λ^0 helicity frame $S_{\Lambda L}$, on the *right* the laboratory frame S_L. $\vec{p}_H$ is the Λ_b^0 momentum, $\vec{p}_p$ is the proton momentum (corresponding to a solid angle (θ', ϕ') in the $S_{\Lambda L}$ frame), $\vec{p}_{\text{beam}}$ is the proton beam momentum, while $\vec{n}_\Lambda$ and $\vec{n}_H$ are the normals to the Λ^0 and Λ_b^0 production planes respectively.

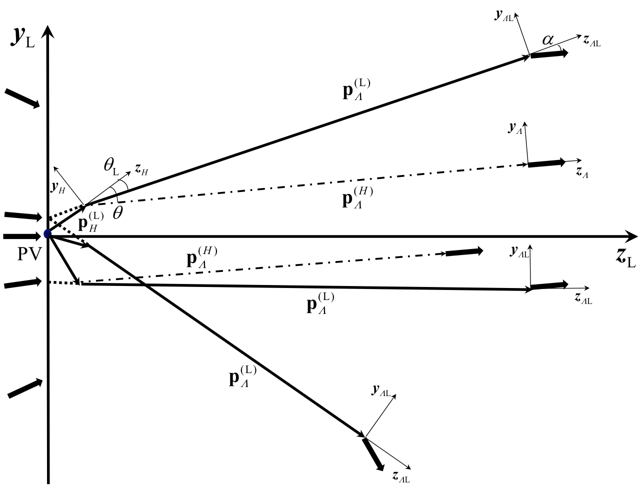

Figure 1.3: Ioboh.

The polarization given by the equation of motion derived in Section 1.3.3 refers to the comoving rest frame of the Λ^0 (also known as the *canonical frame)*, related to the S_L frame by a Lorent boost. By contrast, equation (1.42) for the angular distribution is computed with the solid angle Ω' in the particle helicity frame $S_{\Lambda L}$. Canonical and helicity frames are related by a rotation angle, meaning that $\vec{s_0}$ is not fixed to be perpendicular to $\vec{B}$, as assumed in the resolution of the system (1.31). This effect arises in the case of Λ^0 not directed along the S_L z axis and is expected to be negligible for the purposes of this thesis.

More significant is the Wick rotation, owing to the orientation discrepancy between S_Λ frame (where the Λ^0 has the maximal longitudinal polarization) and $S_{\Lambda L}$ (where the angular distribution of Λ^0 decay products is measured).

This phenomenon introduces a dilution effect to the precession measurement: a Λ^0 with polarization $\vec{s_0} = s_0\hat{z}_\Lambda$ in the S_Λ frame gains in the $\mathrm{S}_{\Lambda\mathrm{L}}$ frame a transverse component of magnitude $s_0 \sin\alpha$, where [28]

$$\sin\alpha = \frac{m_\Lambda}{m_H}\frac{\left|\vec{p}_H^{\,(\mathrm{L})}\right|}{\left|\vec{p}_\Lambda^{\,(\mathrm{L})}\right|} \tag{1.44}$$

and θ is the Λ^0 helicity angle, i.e. the angle formed by the Λ^0 momentum in S_H with respect to the frame z_H axis.

[Rotazione di Wick]

1.4.4 Closing remarks

The LHCb tracking dipole magnet provides an integrated field $D_y \approx \pm 4\,\mathrm{T\,m}$ [29], allowing for a maximum precession angle of $\Phi_{\max} \approx \pm\frac{\pi}{4}$ for Λ^0 baryons traversing the entire region and reaching about 70% of the maximum s_y component in equation (1.39). With the 8 fb^{-1}...

Chapter 2

The LHCb experiment

2.1 The Large Hadron Collider

The Large Hadron Collider (LHC for short) is the largest and most powerful particle collider in the world.

2.2 The LHCb experiment and detector

LHCb (the *b* stands for *beauty*[1]) is one of the four main experiments at the LHC.

Elenca i successi.

RICORDA DI DIRE IL SISTEMA DI COORDINATE! Non usare questo, che è preso da online: A right-handed coordinate system is defined centred on the interaction point, with z along the beam axis and y pointing upwards.

2.2.1 Tracking

VELO

Tracker Turicensis

T stations

Track classification

Qui tutta la storia delle T track

[1]Before settling on the names *top* and *bottom* for the third generation of quarks, the names *truth* and *beauty* were among those proposed. While they never gained enough momentum in the scientific community, echoes of the failed nomenclature are still present in heavy quark vocabulary, for instance in the alternative name *truth* for the *topness* flavour number mentioned in Section 1.1.2, as well as in the official name for the LHCb experiment.

2.2.2 Particle identification

RICH

Calorimeter

Muon system

2.3 The LHCb data flow

Qui trigger, track reconstruction e tutto il resto.

2.4 LHCb detector upgrade for Run 3

2.5 Data

Non so se vada qui ma da qualche parte deve andare.

Chapter 3

Λ_b^0 and Λ^0 decay vertex reconstruction

This chapter details my work towards the improvement of the vertex reconstruction process for decays involving T tracks. Section 3.1 delves into a deep study of the vertexing process at LHCb and the two algorithms employed in this thesis; Section 3.2 introduces the problem of low vertexing efficiency for the decay of interest $\Lambda_b^0 \to J/\psi\ \Lambda^0$; Section 3.3 presents my efforts in the characterization of the non-converged events in search for the root cause of the vertexing falure; finally, Section 3.4 proposes my solution to improve the signal yield through partial recovery of non-reconstructed events.

3.1 Vertex reconstruction algorithms at LHCb

3.1.1 Vertex Fitter algorithm

The Vertex Fitter (VF), implemented as part of the LoKi analysis toolkit, is the main vertexing algorithm used for the reconstruction of the Λ_b^0 decay.

Under VF formalism, each daughter particle is represented by a 7-dimensional vector[1]

$$\vec{p} = \begin{pmatrix} \vec{r} \\ \vec{q} \end{pmatrix} = \begin{pmatrix} r_x \\ r_y \\ r_z \\ p_x \\ p_y \\ p_z \\ E \end{pmatrix}, \tag{3.1}$$

[1] This chapter assumes the standard right-handed LHCb coordinate system, see Section 2.2.

containing its 4-momentum $\vec{q}$ computed at the *reference point* $\vec{r}$. This parameter vector has an associated covariance matrix V, which can be written in block structure as

$$\begin{pmatrix} V_r & V_{rq} \\ V_{rq}^T & V_q \end{pmatrix}. \tag{3.2}$$

It is also convenient to identify its formal inverse matrix $G := V^{-1}$, which has an analogous block form:

$$\begin{pmatrix} G_r & G_{rq} \\ G_{rq}^T & G_q \end{pmatrix} = \begin{pmatrix} V_r & V_{rq} \\ V_{rq}^T & V_q \end{pmatrix}^{-1} \tag{3.3}$$

Taking the daughter particles as inputs, the Vertex Fitter will output the best fit value $\vec{x}$ for the common origin vertex, along with its covariance matrix C and the χ^2 to evaluate the goodness of fit.

The algorithm builds the decay tree from the bottom-up via a «leaf-by-leaf» approach, fitting one vertex at a time (e.g. $J/\psi \to \mu^+\mu^-$, $\Lambda^0 \to p\pi^-$) and then moving upwards (e.g. $\Lambda_b^0 \to J/\psi\ \Lambda^0$). This process is blind to the downstream leaves and only considers kinematic information of the immediate daughter particles, without accounting for momenta and mass constraints.

Iterating paradigm

The basic unit of recursion of the Vertex Fitter is the *iteration*: the algorithm is set to repeat the vertexing process until either a convergence condition is satisfied (see later) or the fit reaches the set number of allowed iterations, 10 by default. In the latter case, a non-convergence error is thrown and the candidate event is discarded.

At the beginning of each iteration, the final vertex covariance matrix C_n^{i-1} from the previous iteration[2] is scaled down by a factor $s^2 = 10^{-4}$:

$$C_0^i = C_n^{i-1} \times s^2. \tag{3.4}$$

The algorithm then performs a *proper transportation*, a dedicated routine in which all daughter particles are extrapolated to the z component of the current (tentative) position of the common production vertex $\vec{x}_n^{i-1}$.

Extrapolation using T tracks is a sensitive affair: unlike the case for other track types, no constraints are available besides the downstream measurement performed by the T tracking stations, meaning the tracks have to be propagated through several meters while accounting for the intense and non-homogeneous LHCb magnetic field. For this analysis, said extrapolation was performed via numerical solution of the track propagation equations using an approach based on the Runge-Kutta (RK) method [30] [31].

[2]The subscript n identifies the final step number, see later.

Step

Within an individual iteration i, denoted by a superscript, the Vertex Fitter algorithm proceeds by *steps* denoted by subscripts, with each step k coinciding with the addition of the k-th daughter particle.

Given information on the vertex position $\vec{x}_{k-1}$ obtained using the first $k-1$ particles, track k is added through the following recursive procedure. First the inverse vertex covariance matrix is updated:

$$C_k^{-1} = C_{k-1}^{-1} + V_{r_k}^{-1}, \tag{3.5}$$

where the reference point inverse covariance matrix $V_{r_k}^{-1}$ has been updated at the beginning of the iteration through the proper transportation phase.

If C_k^{-1} can successfully be inverted, the algorithm updates the current best estimate of the common origin vertex:

$$\vec{x}_k = C_k \left[C_{k-1}^{-1} \vec{x}_{k-1} + V_{r_k}^{-1} \vec{r}_k \right]. \tag{3.6}$$

To conclude the step, the vertex χ^2 is updated to the account for the new position:

$$\begin{aligned} \chi_k^2 = \chi_{k-1}^2 & \\ + (\vec{r}_k - \vec{x}_k)^T V_{r_k}^{-1} (\vec{r}_k - \vec{x}_k) & \quad . \\ + (\vec{x}_k - \vec{x}_{k-1})^T C_{k-1}^{-1} (\vec{x}_k - \vec{x}_{k-1}) & \end{aligned} \tag{3.7}$$

Seeding

As one can observe, the procedure described above requires, at each step, both a previous estimated vertex position $\vec{x}_{k-1}$ and an associated inverse covariance matrix C_{k-1}^{-1}. In particular, step $k = 1$ demands the existence of $\vec{x}_0$ and C_0^{-1}.

For iterations $i > 1$, such roles are handily filled by the final vertex computed during the previous iteration. For the purpose of providing the first step of the first iteration with these values, at the beginning the algorithm tries to extract a *vertex seed*, a first estimate of the decay vertex position, through a dedicated procedure depending on decay topology and properties of particles involved.

In the case of interest of the $\Lambda^0 \to p\pi^-$ two-body decay, said procedure is a simplified step of the Kalman filter:

$$C_0^{-1} = V_{r1}^{-1} + V_{r2}^{-1} \tag{3.8a}$$

$$\vec{x}_0 = C_0 \left(V_{r1}^{-1} \vec{r}_1 + V_{r2}^{-1} \vec{r}_2 \right) \tag{3.8b}$$

Subscripts 1 and 2 as used above refer to the two daughter particles in the decay (i.e. proton and pion).

Termination and smoothing

The two VF convergence conditions are both based on comparisons between the vertex position computed at the end of the current iteration with the one from the previous iteration, with convergence being called if either one of them is satisfied.

The first condition is placed on the absolute distance between the vertices:

$$\left\| \vec{x}_n^i - \vec{x}_n^{i-1} \right\| \leq d_1 \tag{3.9}$$

where $d_1 = 1\,\mu\text{m}$ by default. The second condition, by far the more commonly satisfied one when reaching convergence, is a condition on vertex distance «in χ^2 units»:

$$\left(\vec{x}_n^i - \vec{x}_n^{i-1} \right)^T C_n^{i\,-1} \left(\vec{x}_n^i - \vec{x}_n^{i-1} \right) \leq d_2 \tag{3.10}$$

with $d_2 = 0.01$. While condition (3.9) can be satisfied at any point in the vertexing process, (3.10) convergence additionally requires $i > 1$, thereby excluding the very first iteration.

When convergence is reached, the algorithm applies a smoothing process: for each daughter particle, the reference point $\vec{x}_k$ is fixed to the final vertex position $\vec{x}_n^i$ and the momentum $\vec{q}_k$ is updated accordingly as

$$\vec{q}_k = \vec{q}_n^i - V_{rq_k} V_{r_k}^{-1} \left(\vec{r}_k - \vec{x}_k \right) \tag{3.11}$$

Finally comes the evaluation of the relevant covariance matrices. The vertex covariance matrix C is obviously fixed at C_n^i; the algorithm also computes for each entry the correlation matrix $E_k \coloneqq \operatorname{corr}\left(\vec{x}, \vec{q}_k\right)$ between the vertex position and the particle momentum

$$E_k = -F_k C, \tag{3.12}$$

and the particle momentum covariance matrix

$$D_k = V_{q_k} - V_{rq_k} V_{r_k}^{-1} V_{rq_k}^{\;T} + F_k C F_k^{-1}, \tag{3.13}$$

with

$$F_k = -V_{rq_k} V_{r_k}^{-1} \tag{3.14}$$

being an auxiliary matrix.

Mother particle creation

Assuming the found vertex is inside the LHCb fiducial volume, the fit is validated and a χ^2 is determined by taking the last step value from (3.7) and adding the χ^2 from any short-lived daughter particle. Degrees of freedom (DOFs) for χ^2 reduction are computed as follows:

- each track contributes 2 DOFs;
- each ρ^+-like particle[3] contributes 2 DOFs;
- each sub-vertex contributes 3 DOFs plus further DOFs from the downstream decay tree;
- the sum total is reduced by 3.

A mother particle is subsequently created using the (3.1) representation with reference point $\vec{x}_{\text{mother}}$ fixed to the new-found vertex coordinates. Its 4-momentum is computed as a simple sum of the 4-momenta of its daughters extrapolated at the vertex:

$$\vec{q}_{\text{mother}} = \sum_{k \in \text{daughters}} \vec{q}_k. \tag{3.15}$$

The parameter vector covariance matrix (3.2) is determined as follows:

$$V_r^{\text{mother}} = C, \tag{3.16}$$

$$V_q^{\text{mother}} = \sum_{k \in \text{daughters}} \left[D_k + \sum_{\substack{j \in \text{daughters} \\ j \neq k}} \left(F_k C F_j^T + F_j C F_k^T \right) \right], \tag{3.17}$$

$$V_{rq}^{\text{mother}} = \sum_{k \in \text{daughters}} E_k, \tag{3.18}$$

with D_k, E_k and F_k for each daughter resulting from (3.13), (3.12) and (3.14) respectively.

Finally, the mother particle measured mass M_{mother} is computed as magnitude of 4-vector $\vec{q}_{\text{mother}}$ in the $(-,-,-,+)$ metric

$$M_{\text{mother}} = \sqrt{E_{\text{mother}}^2 - p_{x\,\text{mother}}^2 - p_{y\,\text{mother}}^2 - p_{z\,\text{mother}}^2}, \tag{3.19}$$

Its associated uncertainty is defined as

$$\sigma_M^{\text{mother}} = \sqrt{\frac{1}{4M_{\text{mother}}^2} v^T H v}, \tag{3.20}$$

with

$$v := \frac{dM_{\text{mother}}^2}{d\vec{q}} = \begin{pmatrix} -2p_{x\,\text{mother}} \\ -2p_{y\,\text{mother}} \\ -2p_{z\,\text{mother}} \\ 2E_{\text{mother}} \end{pmatrix} \tag{3.21}$$

[3] A ρ^+-like particle is a particle resulting from the combination of 1 long-lived particle and ≥ 2 photons. The category identifier is owed to the topology of the $\rho^+ \to \pi^+\pi^0$ decay with $\pi^0 \to \gamma\gamma$.

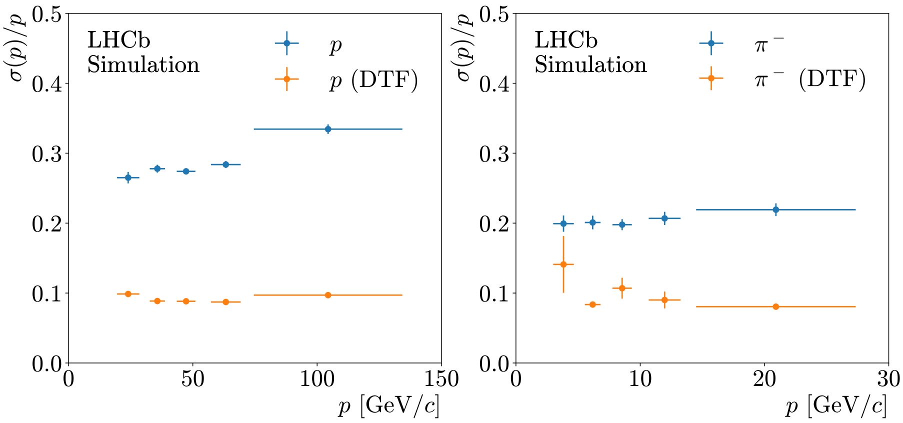

Figure 3.1: Momentum resolution.

and

$$H := \sum_{k \in \text{daughters}} V_{q_k}. \tag{3.22}$$

3.1.2 Decay Tree Fitter algorithm

While the leaf-by-leaf approach adopted by the Vertex Fitter is fast, it brings alongside it the significant drawback of forgoing upstream information when fitting the downstream branches of a decay. This is especially notable for decays like $K_S^0 \to \pi^0\pi^0 \to \gamma\gamma\gamma\gamma$, where the final state has no tracks to form a vertex with. Even in the relatively more traditional case of the $\Lambda_b^0 \to J/\psi\ \Lambda^0$ decay, however, the VF algorithm still limits our options. In particular, it prevents the placing of *mass constraints* on mother particles, where the fit fixes the invariant mass of the $p\pi^-$ pair to the PDG value for $m(\Lambda^0)$, for instance.

To combat this problem, all reconstructed events in this analysis undergo a refit process based on the Decay Tree Fitter (DTF) algorithm [32] first developed in BaBar. This algorithm takes the entire decay chain as input and allows to place mass constraints on $p\pi^-$ and $\mu^+\mu^-$ invariant masses to match $m(\Lambda^0)$ and $m(J/\psi)$ respectively.

While this step introduces another filtering process and related efficiency to account for[4], it proves invaluable for our physics motivations as it mitigates the most problematic drawback of T track usage, momentum resolution. As shown

[4]DTF convergence efficiency with the double mass constraint is relatively uneven across the $z_\Lambda^{\texttt{vtx}}$ spectrum, starting at $\approx 50\%$ for $z_\Lambda^{\texttt{vtx}} \approx 6\,\text{m}$ and growing up to $\approx 85\%$ for $z_\Lambda^{\texttt{vtx}} \approx 7.5\,\text{m}$. Comparably, vertex reconstruction is still the primary cause of event loss in this analysis.

in Figure 3.1, using both J/ψ and Λ^0 mass constraints improves $\vec{p}$ resolution from $20 \div 30\%$[5] to $\approx 10\%$.

3.2 Reconstruction efficiency of the Λ_b^0 and Λ^0 decays

To compute the vertex reconstruction efficiency for the Λ_b^0 decay chain, it is useful to conceptualize our event selection as a five step process:

1. reconstruction of associated tracks for all charged daughter particles;
2. reconstruction of the three decay vertices (Λ^0, J/ψ and Λ_b^0);
3. preliminary selections based on kinematic variables to filter out most background (see Section 4.1);
4. Decay Tree Fitter refit with appropriate mass constraints for the analysis at hand (usually J/ψ and Λ^0);
5. further selections applied to events passing all previous steps. Detailed in Chapter 4, these include a physical background veto and signal selection via a trained multivariate classifier.

For the purposes of this section, we are interested in the first two steps (track and vertex reconstruction).

Efficiencies are computed with respect to *reconstructible* particles, a flag attributed during the simulation process based on the number of *hits* (charged clusters with defined positions) in specific modules of the LHCb detector. A track is said to be reconstructible as VELO track with hits in ≥ 3 VELO modules, while it's reconstructible as T track with ≥ 1 hits in both the x and stereo layers of each T station. If these conditions are satisfied simultaneously, the track qualifies for reconstructibility as Long track [33].

At Monte Carlo level, a track is deemed to be *reconstructed* if it can be successfully matched to at least one MC particle; for T and Long tracks, this is true if at least 70% of the hits from the respective relevant detectors for reconstructibility are shared between reconstructed and true track. For Λ_b^0 events with a true $z_{\text{vtx}}^{\Lambda} \in [6.0\,\text{m}, 7.6\,\text{m}]$, this results in a track reconstruction efficiency in the 60% to 80% range.

[5] Pion momentum resolution is higher because the pion receives a smaller fraction of the Λ^0 momentum, thereby having a larger bending curve than the proton and allowing for better momentum measurement at the T stations.

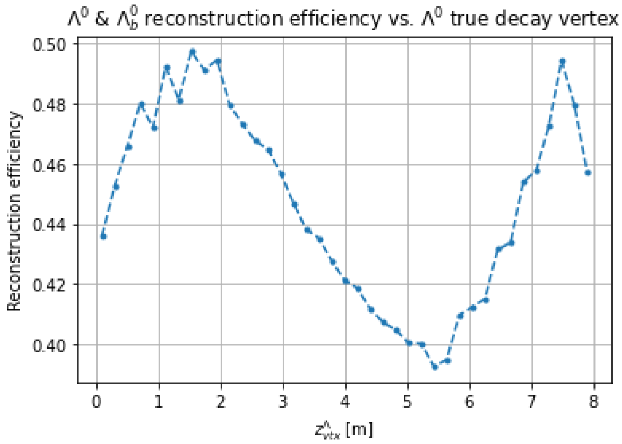

Figure 3.2: Reconstruction efficiency of simulated $\Lambda_b^0 \to J/\psi\ (\to \mu^+\mu^-)\ \Lambda^0\ (\to p\pi^-)$ events as function of the z component of the true Λ^0 decay vertex. Assuming a $\approx 100\%$ reconstruction rate for the J/ψ decay, the low efficiency is attributed to failure in reconstructing Λ^0 and Λ_b^0 decay vertices.

When considering how many of these reconstructed charged particles pass the vertex reconstruction (*vertexing*) process, the computed efficiency is much lower. Figure 3.2 plots the resulting Λ_b^0 vertexing efficiency through the whole true z_{vtx}^{Λ} spectrum, showing that said efficiency never manages to get past the 50% threshold. This means that over half of our candidate signal events is lost during the second step of the five step selection process.

While available information does not distinguish between the three individual vertexing phases (J/ψ, Λ^0 and Λ_b^0), we can make some reasonable assumptions. Being Long tracks, muons and antimuons have well reconstructed momentum with constraints across the LHCb detector; for this reason their influence on the vertexing efficiency dip is considered negligible. Furthermore, the rare usage of T tracks for physics analysis in LHCb suggests that problems are likelier to arise in the $\Lambda^0 \to p\pi^-$ vertexing and then cascade into the $\Lambda_b^0 \to J/\psi\ \Lambda^0$ reconstruction.

For the above reasons, in the following sections I'll focus on the $\Lambda^0 \to p\pi^-$ decay to search for issues and solutions, with the goal of improving signal yield.

3.3 Characterization of non-converged events

3.3.1 Behaviour through VF iterations

The VF process reaches convergence if either condition (3.9) or (3.10) is satisfied, i.e. if the vertex position estimated at iteration i and the one from

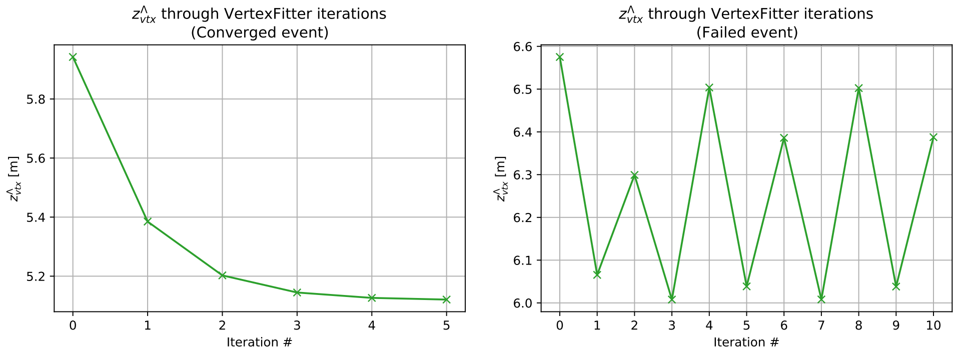

(a) **(b)**

Figure 3.3: Left right

iteration $i-1$ are «close enough» either in absolute distance or χ^2 distance, up until $i_{\max} = 10$. This is predicated on the principle that the algorithm refines its vertex estimate after each iteration, homing in on the candidate vertex with the lowest $\tilde{\chi}^2_{\text{vtx}}$.

Such a behaviour is not found in non-converging (henceforth also known as *failed*) events. This can be seen by increasing $i_{\max} = 100$, which causes a negligible $\approx 2\%$ increase in converged events. It follows that, for the vast majority of missing events, failure of convergence is not a product of low computation time and must instead result from some internal malfunction of the vertexing process.

This is readily apparent when studying the vertex positions throughout the iterating process for examples of converged and failed events of simulated signal. Figure 3.3 compares the values of z^{vtx}_{Λ}, the z component of the $\Lambda^0 \to p\pi^-$ decay vertex, as reconstructed by the VF in iterations 0 to 10 ($i = 0$ being the starting seed). Figure 3.3a (converged) exhibits the expected behaviour, with the algorithm refining its vertex estimate after every iteration and finally converging as early as $i = 5$. By contrast, Figure 3.3b (failed) presents an *oscillating behaviour* of z^{vtx}_{Λ}, constantly flipping the probing direction after an iteration completes. While a particularly tricky instance of the first type of event may potentially benefit by an increased $i_{\max}$, no amount of allotted computations can lead the second type to convergence.

Some more insight into the nature of this oscillation can be achieved by taking a more «geometrical» look, plotting inter-iteration vertex coordinates in the zx plane where the LHCb magnet bends tracks according to their charge. Figure 3.4 compares the same events from Figure 3.3. Again, the converged event in Figure 3.4a behaves as intended, selecting as vertex roughly the point of closest distance between the tracks (some leeway is accorded since the fit

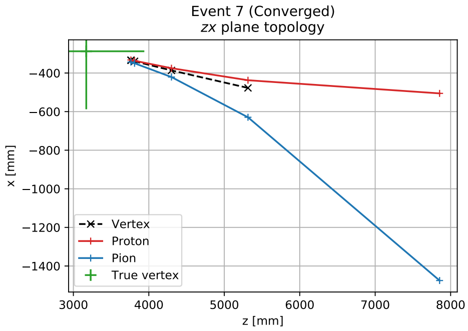

(a)

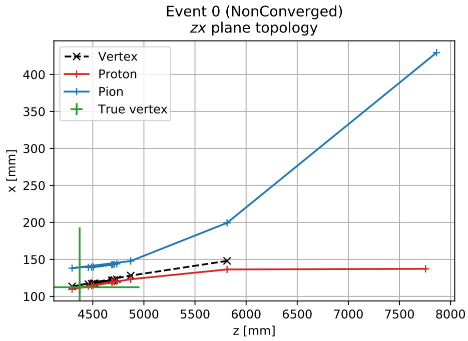

(b)

Figure 3.4: Dovrebbero essere gli stessi eventi della figura precedente, altrimenti non è elegante.

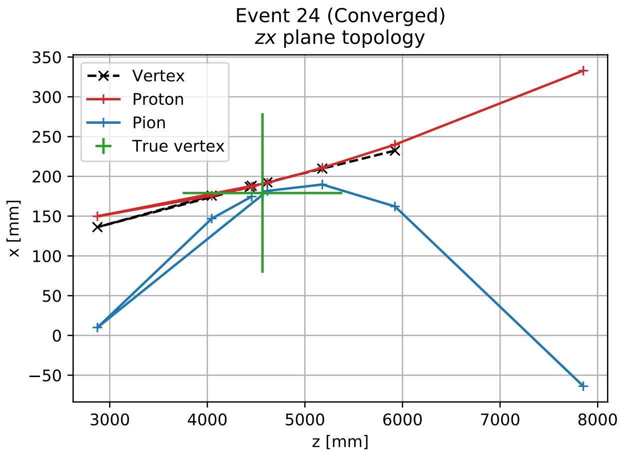

Figure 3.5: A.

also incorporates information from xy and yz planes). The progress in Figure 3.4b is more interesting: in the failed case the estimated vertex, identified at each iteration by «x» markers along the dashed line, appears to gravitate *around* the point of closest distance, never outright choosing it as candidate. Significantly, the *true* Λ^0 vertex (marked by the green cross) lags some 50 cm behind it.

While it may be tempting to attribute the failed convergence to the comparably larger gap between proton and pion tracks at their point of closest distance, some observations are in order: first, the deceivingly different x scales in Figures 3.4a and 3.4b mean that in the latter tracks are closer than they may seem; more to the point, the VF algorithm has shown to be capable of bridging an imperfect track extrapolation in converged events, as demonstrated in

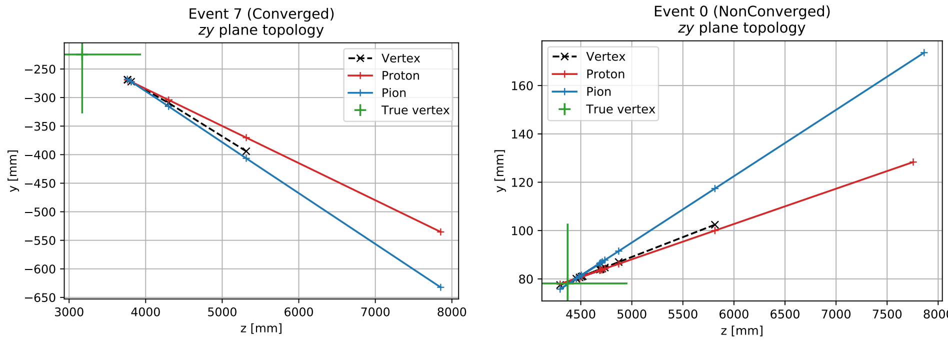

(a) **(b)**

Figure 3.6: Devono essere gli stessi eventi della figura precedente, altrimenti non ha senso lol.

Figure 3.5.

We can make a more convincing remark by analyzing performance in the yz plane, where tracks *don't* bend. Figure 3.6a shows that, in the converged case, the yz track crossing is z-aligned with the closest xz distance point. This doesn't happen for the failed event: while Figure 3.6b shows that yz tracks cross almost coinciding with the true vertex position, we have already pointed out that this is 50 cm short of the xz closest distance point. Convergence failure for the event in Figures 3.4b and 3.6b can thus be interpreted through the lens of *conflicting information*: the best vertex candidate has different z_{vtx} in the xz (with magnetic field) and yz (without magnetic field) planes, and the VF algorithm flip-flops between the two.

For didactic purpose, the analysis in this section has focused on just one event. All the emerged patterns are however commonplace throughout the failed events I have examined, with the oscillating vertex behaviour in particular being a constant in almost all of them. While every Λ_b^0 vertexing failure being the fault of xz and yz track mismatch would be a reckless conclusion, I have been able to use these findings, along with other from the following paragraphs, to devise a partial solution in Section 3.4.2.

3.3.2 True kinematics

To further investigate the possible source of the oscillating behaviour outlined in Section 3.3.1, I have conducted a systematic comparison of kinematic features at Monte Carlo level between converged and failed events.

No difference among the two categories emerge when considering basic decay descriptors such as the momenta of all particles involved and the decay vertices of unstable particles. Moreover, there doesn't seem to be a critical

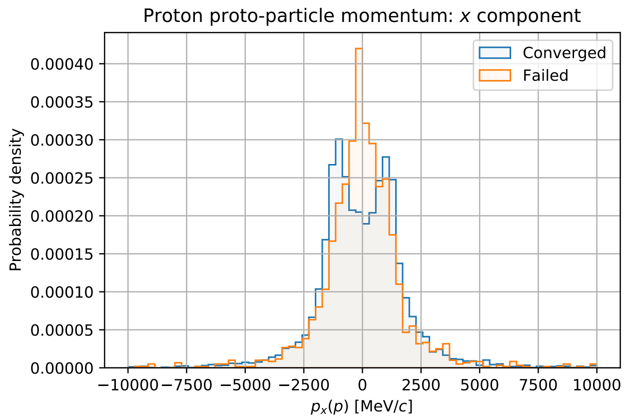

Figure 3.7: A.

decay geometry that triggers the vertexing; for instance, there is no evidence that $\Lambda^0 \to p\pi^-$ decays lying largely in the xz plane, a setup quite unfriendly to the VF algorithm (see Section 4.1.1), has any disproportionate representation amongst non-converged events.

3.3.3 Kinematics at first measurement position

A major discrepancy emerges when looking at particle interaction with the detector via *protoparticles*. A protoparticle is a data structure created during the LHCb event reconstruction process with the intent of encapsulating all relevant information available for the associated particle: particle identification (PID) from the RICH and muon detectors, results from calorimeter hits and track information. The latter contains details on momentum in relation to a certain reference point which, for stable charged particles, corresponds to the position of first measurement.

In the case of simulated protons from $\Lambda_b^0 \to J/\psi\ \Lambda^0$ decays, the distribution of the protoparticle p_x for converged and failed events shows a marked difference outlined in Figure 3.7: correctly reconstructed events tend to have a double peak roughly centered in $\approx \pm 1$ GeV, while missing events have a more traditional single peak centered in 0.

Even more interestingly, this discrepancy can be put in relation to the y component of the protoparticle first measurement position, as seen in Figure 3.8. The ring-like structure in Figure 3.8 implies that the vertexing process struggles to reconstruct proton protoparticles with low p_x hitting the T stations at $y \approx 0$. No such discrepancy is present in the case of pions.

A precise estimate of p_x is of paramount importance for correct track measurement and extrapolation. Even slight mistakes in angle assessment are mag-

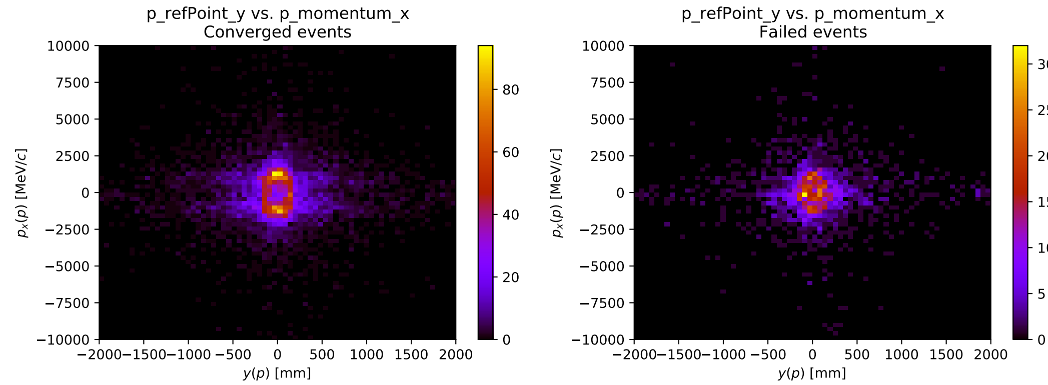

Figure 3.8: B.

nified during particle transportation through long distances, especially since the T track requirement leaves no upstream constraints. Moreover, momentum itself is computed through evaluation of the particle bending curve in the xz plane induced by the magnet. As such, it stands to reason that poor measurement of the low proton p_x can have enough of an effect to throw off the vertexing algorithm.

3.3.4 Kinematics at true vertex

As will be later discussed in Sections 3.4.2 and 4.1.1, reconstruction of the Λ^0 vertex is affected by a significant positive bias of median value $\mu_{\frac{1}{2}}\left(z_\Lambda^{\text{reco}} - z_\Lambda^{\text{true}}\right) \approx$ 43 cm. In spite of such a discrepancy, the standard modus operandi for kinematics-at-vertex analyses usually compares the true momenta (evaluated at the true vertex) with the reconstructed momenta (evaluated at the reconstructed vertex).

For this section I have followed a different approach, instead opting to transport via Runge-Kutta extrapolator the reconstructed p and π^- at the true $\Lambda^0 \to p\pi^-$ vertex position, injected from Monte Carlo information. Since the extrapolator takes raw protoparticles as inputs, this process bypasses any smoothing applied during the fit process and, given an observable f (particle reference points and momenta, for instance), it allows for a comparison between the true value f_{true} and the RK-extrapolated value f_{RK} at the actual z_Λ^{vtx}, circumventing the effect of vertex bias. Any potential mismatch will be normalized in terms of *residuals*

$$\text{res}(f) := \frac{f_{\text{RK}} - f_{\text{true}}}{\sigma_f^{\text{RK}}}, \tag{3.23}$$

with σ_f^{RK} being the uncertainty computed by the RK algorithm. Assuming

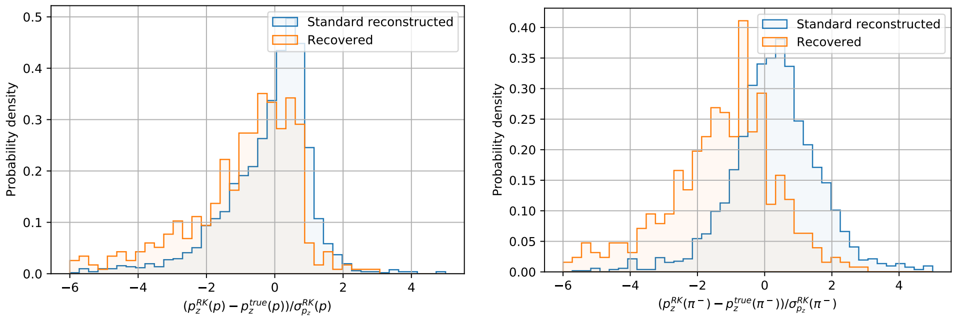

(a) (b)

Figure 3.9: Left right

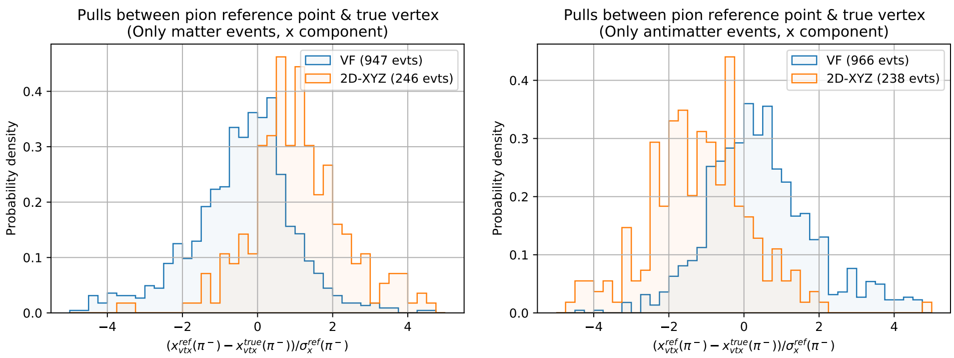

(a) (b)

Figure 3.10: Left right

a correct estimation of such uncertainties, we expect the residuals to follow a standard normal distribution.

Figure 3.9 shows p_z residuals for proton and pions extrapolated at the Λ^0 true decay vertex, juxtaposing converged and non-converged event distributions. The first takeaway is that VF-reconstructed events have a remarkably non-gaussian distribution, with a slightly positive mean and asymmetric tails. This is particularly apparent in the case of the proton, where for $p_z^{\mathrm{RK}} < p_z^{\mathrm{true}}$ the RK algorithm systematically underestimates the error. More relevant for this chapter is Figure 3.9b specifically, which highlights the fact that pion tracks from non-converged events generally sport a strong negative bias on p_z.

This behaviour can also be observed from a different perspective by considering the pion reference point x residuals[6], plotted in Figure 3.10. For this part of the analysis, we forgo the established omission of charge-conjugate notation and separate events in matter ($\Lambda^0 \to p\pi^-$) and antimatter ($\bar{\Lambda}^0 \to \bar{p}\pi^+$) events. Since all events in this sample have magnet polarity $M_{\text{pol}} = +1$, i.e. magnetic field flowing towards the positive direction of the y axis, matter and antimatter daughter particles will bend in opposite directions due to charge inversion.

Comparing Figures 3.10a and 3.10b, x components of pion reference points in non-converged events show opposite bias when extrapolated at the Λ^0 vertex. Such a behaviour is easily understood in terms of transportation: tracks are extrapolated from downstream protoparticles towards decreasing z; if the magnetic bending effect in the zx plane is overstated (if tracks «bend too much»), the resulting x reference point at true z_Λ^{vtx} will have an offset with respect to the actual origin vertex of the particle with polarity-depdendent sign (cf. Figure 3.4b).

Excessive bending is exactly what is expected of a track with correctly estimated p_x and p_y, but underestimated p_z. Furthermore, a lower p_z will affect the closest distance point between proton and pions in the zx plane, but will have a much lower impact on the track crossing point in the yz plane, supporting the conflicting information interpretation for vertex oscillation given in Section 3.3.1. Considering the information gathered so far, the two most plausible causes of failed convergence appear to be wrong extrapolation by the Runge-Kutta algorithm, perhaps triggered by lower protoparticle p_x observed in Section 3.3.3, and/or poor measurement from T stations resulting in p_z underestimation of protons and pions.

3.4 Recovery of non-converged events

3.4.1 Recovery through interpolation

@todo

3.4.2 Recovery through refit with rescaled uncertainties

As outlined in Section 3.3.1, vertexing failures in the $\Lambda^0 \to p\pi^-$ decay can be attributed to candidate vertices in different planes providing conflicting information. In order to circumvent this phenomenon, my proposal for the

[6]The Runge-Kutta extrapolator transports a particle up to a specified z coordinate. As a consequence, x and y reference points gauge the discrepancy between track extrapolation and the true position of the MC particle at said z, with $z_{\text{ref}}^{\text{RK}} \approx z_{\text{ref}}^{\text{true}}$ within extrapolator tolerance.

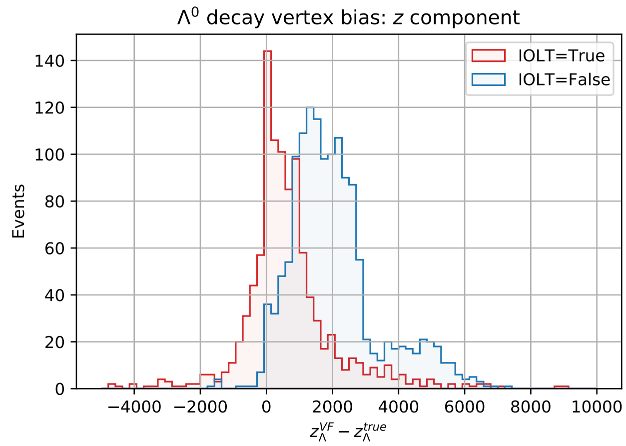

Figure 3.11: A.

recovery of these failed events involves performing a refit process with a slightly altered version of the standard Vertex Fitter, designed to give more importance to tracks lying on a specific plane.

The obvious choice for said plane is the yz plane, since extrapolation of these tracks does not need to be concerned with magnet bending and is therefore expected to be less prone to error. However, this would penalize events with poor yz protoparticle reconstruction, for instance events with parallel or diverging tracks in said plane. To maximize the recovery efficiency of my solution, I have elected to perform three separate refits on non-converging events, prioritizing $yz \to xz \to xy$ planes in this order. In a worst-case scenario, this would quadruple the time complexity of the vertexing process; in practice, half of all events converge with the standard VF, and about $\approx 15\%$ more converge after the first refit attempt (yz plane).

Considering the yz plane as an example, we can prioritize available information for tracks in this plane by artificially increasing the uncertainty σ_x for the x component of the candidate vertex position $\vec{x}$. At each step in a VF iteration, $\vec{x}$ is updated according to (3.6). Uncertainties enter the computation through three terms:

1. C_{k-1}^{-1}, inverse $\vec{x}$ covariance matrix computed at the previous step (or previous iteration);

2. V_{rk}^{-1}, inverse covariance matrix of reference point $\vec{r}_k$, computed at the true transport of particle k;

3. C_k, current $\vec{x}$ covariance matrix, inverted from the matrix sum of the previous two terms as in (3.5).

Ergo, the best approach to increase σ_x while minimizing additional computation time is to act on the individual components of C_{k-1}^{-1} and $V_{r\,k}^{-1}$ just before the (3.5) sum.

Assuming gaussian uncertainties, a standard three-dimensional covariance matrix will have the form

$$C = \begin{pmatrix} \sigma_x^2 & \rho_{xy}\sigma_x\sigma_y & \rho_{xz}\sigma_x\sigma_z \\ \rho_{xy}\sigma_x\sigma_y & \sigma_y^2 & \rho_{yz}\sigma_y\sigma_z \\ \rho_{xz}\sigma_x\sigma_z & \rho_{yz}\sigma_y\sigma_z & \sigma_z^2 \end{pmatrix}, \tag{3.24}$$

where $\rho_{ij} \coloneqq \mathrm{corr}(i, j)$. Its inverse matrix is written as

$$C^{-1} = \frac{1}{K} \begin{pmatrix} \frac{1-\rho_{yz}^2}{\sigma_x^2} & \frac{\rho_{xz}\rho_{yz}-\rho_{xy}}{\sigma_x\sigma_y} & \frac{\rho_{xy}\rho_{yz}-\rho_{xz}}{\sigma_x\sigma_z} \\ \frac{\rho_{xz}\rho_{yz}-\rho_{xy}}{\sigma_x\sigma_y} & \frac{1-\rho_{xz}^2}{\sigma_y^2} & \frac{\rho_{xy}\rho_{xz}-\rho_{yz}}{\sigma_y\sigma_z} \\ \frac{\rho_{xy}\rho_{yz}-\rho_{xz}}{\sigma_x\sigma_z} & \frac{\rho_{xy}\rho_{xz}-\rho_{yz}}{\sigma_y\sigma_z} & \frac{1-\rho_{xy}^2}{\sigma_z^2} \end{pmatrix}, \tag{3.25}$$

with

$$K \coloneqq \frac{\det C}{\sigma_x^2\sigma_y^2\sigma_z^2} = 1 + 2\rho_{xy}\rho_{xz}\rho_{yz} - \rho_{xy}^2 - \rho_{xz}^2 - \rho_{yz}^2. \tag{3.26}$$

Going back to the yz plane example, we increase σ_x by introducing a multiplicative factor $s_x < 1$ for relevant covariance matrix components as follows:

$$\begin{aligned} C_{xx}^{-1} &= C_{xx}^{-1} \times s_x^2, \\ C_{xy}^{-1} &= C_{yx}^{-1} = C_{xy}^{-1} \times s_x, \\ C_{xz}^{-1} &= C_{zx}^{-1} = C_{xz}^{-1} \times s_x, \end{aligned} \tag{3.27}$$

with other components left as is. This process is also applied to $V_{r\,k}^{-1}$ and replicated at each step of the refit algorithm, which I'll refer to as *σ_x-rescaled*. Similarly, the σ_y-rescaled and σ_z-rescaled algorithms prioritize planes xz and xy respectively; their extension from (3.27) should be trivial. For the remainder of this section, I'll also refer to their sequential application $\sigma_x \to \sigma_y \to \sigma_z$ as the *σ-rescaled refit process*, unless otherwise stated.

As proof of concept, I have analyzed the performance of the σ-rescaled refit approach with $s_i = 0.98, i \in \{x, y, z\}$ (corresponding to $\approx 2\%$ increase in vertex uncertainties) on a sample of [@todo:how many] MC-generated $\Lambda_b^0 \to J/\psi\ \Lambda^0$ events, observing a +25% increase in reconstructed events. As per Figure 3.2, this amounts to about a quarter of all reconstructible events.

I have also run each algorithm individually after the standard VF to gauge their performance on the $n_{\mathrm{tot}}^{\mathrm{reco}}$ recovered events. Results of this test are compiled in Table 3.1. When considering the *recovery efficiency* of each algorithm,

Increased σ	Recovery eff.	$\mu_{\frac{1}{2}}\,[\tilde{\chi}^2_{\text{vtx}}]$	$\mu_{\frac{1}{2}}\,[z_\Lambda^{\text{vtx}}\text{ bias}]$	$\mu_{\frac{1}{2}}\,\left[p_z^{\text{DTF}}(p)\text{ bias}\right]$
None (VF)	–	1.0	429 mm	+1.35%
σ_x	62%	4.9	584 mm	−0.84%
σ_y	74%	5.4	635 mm	−0.81%
σ_z	80%	7.8	697 mm	−1.02%
Sequential	100%	6.5	646 mm	−0.93%

Table 3.1: Performance comparison of the three rescaled-σ algorithms with $s_i = 0.98$ (see text for details), contrasted with the performance of their sequential application ($\sigma_x \to \sigma_y \to \sigma_z$) and the standard Vertex Fitter algorithm. Recovery efficiency is defined as the ratio of events reconstructed by a certain flavour over the total number of events recoverable by combining the three algorithms. $\mu_{\frac{1}{2}}$ identifies the median value. Performances for xyz algorithms are computed using all events recovered by the individual flavour, including events recovered by more than one, while values for VF are computed on standard reconstructed events.

defined as the fraction of recovered events converging under said algorithm, i.e.

$$\varepsilon_i^{\text{reco}}\big|_{i\in\{x,y,z\}} = \frac{n_i^{\text{reco}}}{n_{\text{tot}}^{\text{reco}}}, \tag{3.28}$$

the σ_z-rescaled is the better performing one, reaching convergence in $\approx 80\%$ of recoverable events. Despite this, all three σ-rescaled algorithms have a sizable number of «exclusive» events that do not reach convergence under any other variation. Furthermore, while the σ_z-rescaled does recover more events by itself, only $\approx 5\%$ of the total recovered events are exclusive to it, meaning its overall impact on the σ-rescaled refit process is low.

The established $\sigma_x \to \sigma_y \to \sigma_z$ refit order is justified in light of performance evaluation based on the goodness of these fits. As seen again in Table 3.1, the σ_x-rescaled algorithm has comparably lower vertex $\tilde{\chi}^2$, z_Λ^{vtx} bias and proton p_z bias using the DTF algorithm with J/ψ and Λ^0 mass constraints. Using the σ_z-rescaled algorithm as last resort means only $\approx 5\%$ of recovered events are actually affected by its poor performance.

All σ-rescaled algorithms still appear to perform significantly worse than the standard VF on all the above fronts. To investigate this, I have individually run the σ_x-rescaled and standard VF algorithms on all available events and compared their results. Considering the total number of events reconstructed by combining the two, $\approx 74\%$ of them are reconstructed by both, $\approx 13\%$ are only reconstructed by the σ_x-rescaled (these are the σ_x-recovered events from Table 3.1) and a roughly equal $\approx 13\%$ of them are only reconstructed by the Vertex Fitter.

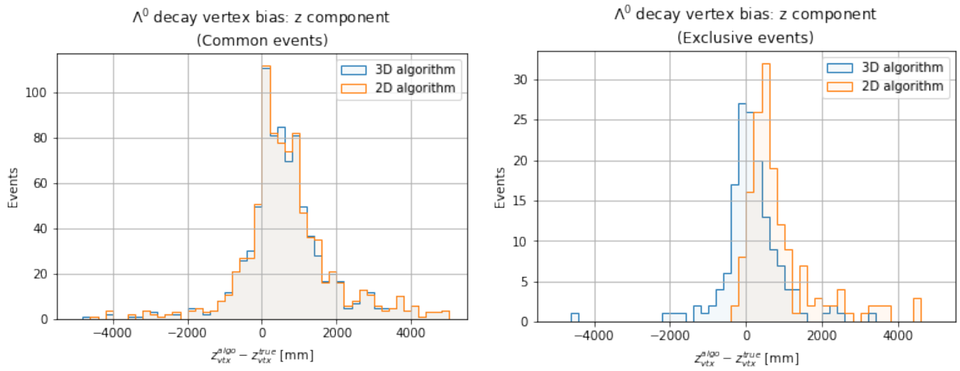

(a) **(b)**

Figure 3.12: Left right

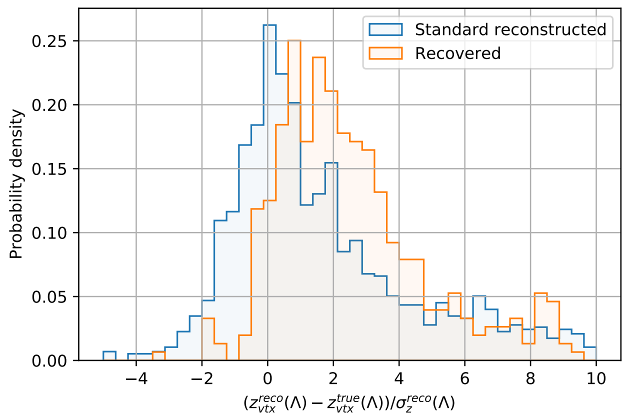

Figure 3.13: A.

What's more interesting is the performance comparison. Figure 3.12a shows the z_Λ^{vtx} bias on events common to VF and σ_x-rescaled. Despite the median 15 cm discrepancy reported in Table 3.1, the two distributions are indistinguishable from the other. The expected difference only emerges when considering events exclusive to each algorithm, as seen in Figure 3.12b.

The differences in z_Λ^{vtx} and proton p_z^{DTF} bias are therefore to be understood in terms of what events reach convergence with a specific algorithm, rather than as performance evaluations of the algorithm itself. The σ_x-rescaled algorithm does not intrinsically reconstruct events with larger bias; instead, its yz-centric approach allows it to recover events that throw off the standard VF, and these events tend to have a larger z_Λ^{vtx} bias on their best vertex candidate. This tendency is likely the result of the systematic T track p_z underestimation analyzed in Section 3.3.3.

Overall, my σ-rescaled refit process proposal allows for the recovery of an extra +25% of signal events. While $\tilde{\chi}^2_{\rm vtx}$ and bias on $z_\Lambda^{\rm vtx}$ are higher compared to events reconstructed via Vertex Fitter (see Figure 3.13 and Table 3.1), there is sufficient evidence pointing towards this being a problem intrinsic to the non-converged events themselves. Their impact on the prospective Λ^0 EDM/MDM measurement will have to be evaluated in dedicated sensitivity studies and possibly incorporated as a source of systematic uncertainty to be accounted for.

Chapter 4

Signal event selection

4.1 Prefiltering

I grafici necessari probabilmente ha senso metterli qui. Magari puoi cambiare il nome in "prefiltering and data characteristics".

4.1.1 Bias in Λ^0 decay vertex

Qui devi menzionare l'orizzontalità, perché vi faccio riferimento nel Cap. 3. Devi dire che c'è il problema con grafico.

4.2 HBDT classifier

4.2.1 Training data

4.2.2 Hyperparameter optimization and performance test

4.2.3 Threshold optimization

4.3 Physical background veto

4.4 Performance on data

Gli invariant mass fits, essenzialmente.

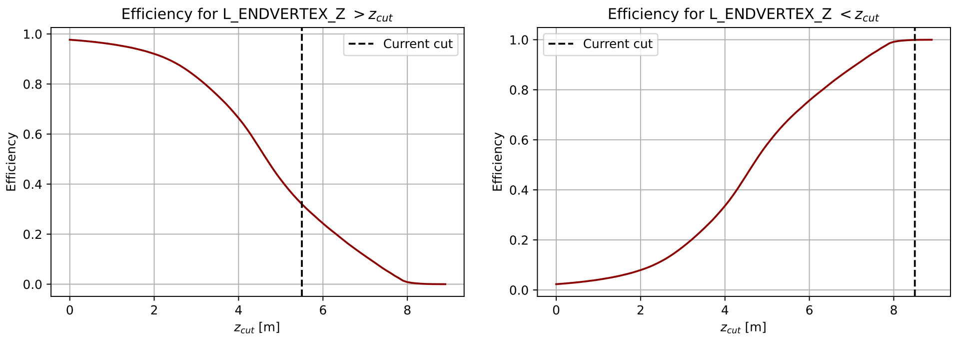

(a) **(b)**

Figure 4.1: Boh...

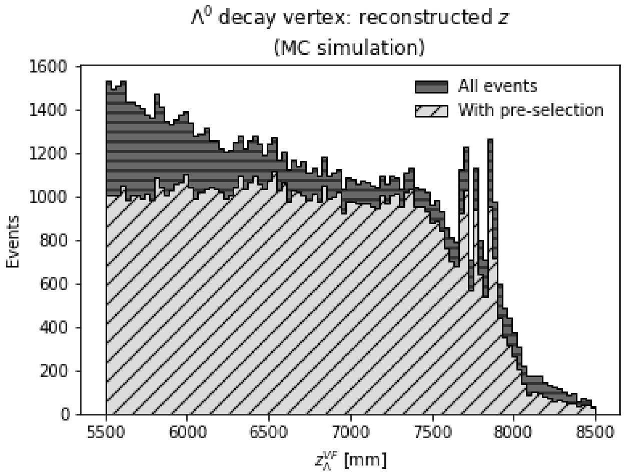

Figure 4.2: Distribution of reconstructed $z_{\Lambda}^{\mathrm{vtx}}$ in simulated $\Lambda_b^0 \to J/\psi\ \Lambda^0$ events, without (*dark grey*) and with (*light grey*) prefiltering.

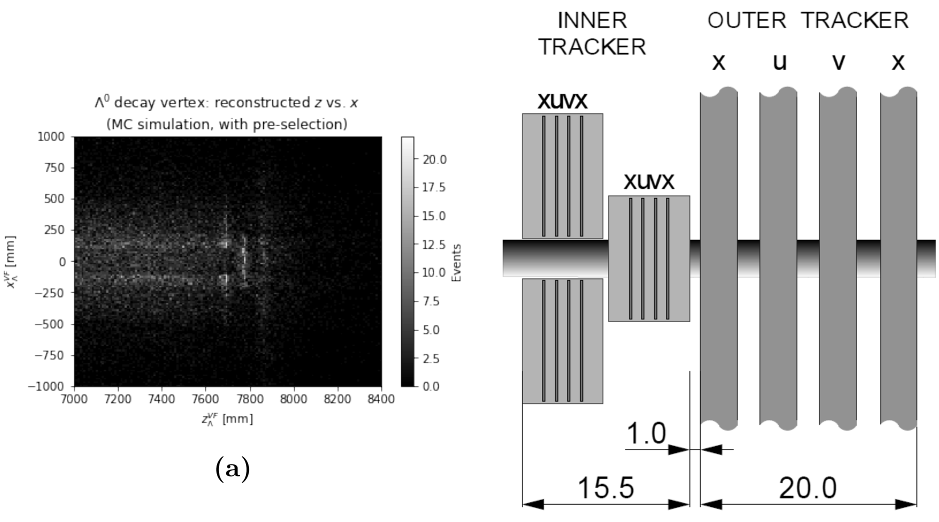

(a)

(b)

Figure 4.3: *Left*: event distribution of simulated Λ_b^0 signal events as a function of reconstructed x_Λ^{vtx} and z_Λ^{vtx}. *Right*: top view diagram of a T tracking station (dimensions along the beam axis given in cm, lateral dimensions not to scale) [34].

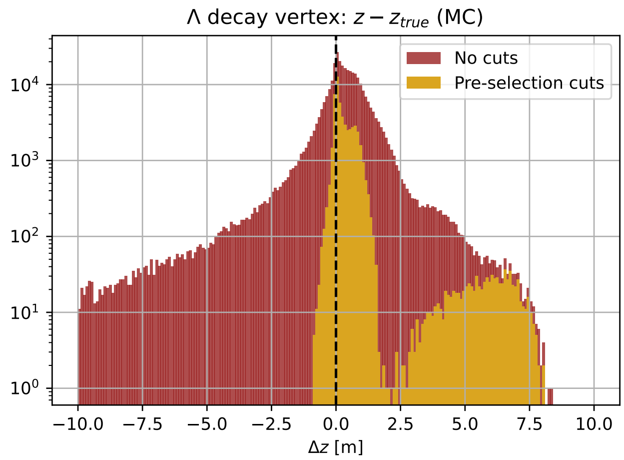

Figure 4.4: Sarebbe meglio mettere immagini vicine, logscale a dx e non-log a sx.

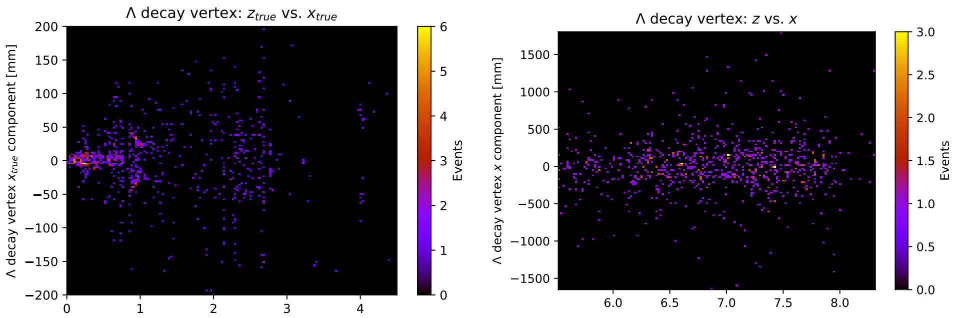

(a) **(b)**

Figure 4.5: Boh...

Appendix A

Angular distribution of $\Lambda^0 \to p\pi^-$ decay products

A.1 Helicity formalism

[Il Richman.]

A.2 Computation of the angular distribution

Bibliography

[1] I. J. R. Aitchinson and A. J .G. Hey. *Gauge Theories in Particle Physics: A Practical Introduction. Volume 1: From Relativistic Quantum Mechanics to QED*. CRC Press, 2013.

[2] J. Erler and M. Schott. Electroweak precision tests of the Standard Model after the discovery of the Higgs boson. *Progress in Particle and Nuclear Physics*, 106:68–119, May 2019.

[3] P. A. Zyla et al. Review of Particle Physics. *PTEP*, 2020(8):083C01, 2020.

[4] A. B. McDonald. Sudbury Neutrino Observatory results. *Physica Scripta*, T121:29–32, Jan 2005.

[5] S.-K. Choi et al. (Belle Collaboration). Observation of a narrow charmonium-like state in exclusive $B^{\pm} \to K^{\pm}\pi^{+}\pi^{-}J/\psi$ decays. *Physical Review Letters*, 91(26), Dec 2003.

[6] T. Nakano et al. (LEPS Collaboration). Evidence for a narrow $S = +1$ baryon resonance in photoproduction from the neutron. *Phys. Rev. Lett.*, 91:012002, Jul 2003.

[7] P. W. Higgs. Broken symmetries and the masses of gauge bosons. *Phys. Rev. Lett.*, 13:508–509, Oct 1964.

[8] G. Aad et al. (ATLAS Collaboration). Observation of a new particle in the search for the Standard Model Higgs boson with the ATLAS detector at the LHC. *Physics Letters B*, 716(1):1–29, Sep 2012.

[9] S. Chatrchyan et al. (CMS Collaboration). Observation of a new boson at a mass of 125 GeV with the CMS experiment at the LHC. *Physics Letters B*, 716(1):30–61, Sep 2012.

[10] J. Zupan. Introduction to flavour physics. *arXiv e-prints*, 2019.

[11] M. S. Sozzi. *Discrete symmetries and CP violation: from experiment to theory.* Oxford University Press, 2013.

[12] C. S. Wu, E. Ambler, R. W. Hayward, D. D. Hoppes, and R. P. Hudson. Experimental test of parity conservation in beta decay. *Phys. Rev.*, 105:1413–1415, Feb 1957.

[13] R. L. Garwin, L. M. Lederman, and M. Weinrich. Observations of the failure of conservation of parity and charge conjugation in meson decays: the magnetic moment of the free muon. *Phys. Rev.*, 105:1415–1417, Feb 1957.

[14] I. B. Khriplovich and S. K. Lamoreaux. *CP Violation Without Strangeness. Electric Dipole Moments of Particles, Atoms, and Molecules.* Springer, 1997.

[15] J. H. Christenson, J. W. Cronin, V. L. Fitch, and R. Turlay. Evidence for the 2π decay of the K_2^0 meson. *Phys. Rev. Lett.*, 13:138–140, Jul 1964.

[16] A. Alavi-Harati et al. (KTeV Collaboration). Observation of direct CP violation in $K_{S,L} \to \pi\pi$ decays. *Physical Review Letters*, 83(1):22–27, Jul 1999.

[17] B. Aubert et al. (BaBar Collaboration). Measurement of CP-violating asymmetries in B^0 decays to CP eigenstates. *Physical Review Letters*, 86(12):2515–2522, Mar 2001.

[18] K. Abe et al. (Belle Collaboration). Observation of large CP violation in the neutral B meson system. *Physical Review Letters*, 87(9), Aug 2001.

[19] L. Canetti, M. Drewes, and M. Shaposhnikov. Matter and antimatter in the Universe. *New Journal of Physics*, 14(9):095012, Sep 2012.

[20] G. Steigman. Primordial nucleosynthesis in the precision cosmology era. *Annual Review of Nuclear and Particle Science*, 57(1):463–491, Nov 2007.

[21] L. Henry, D. Marangotto, A. Merli, N. Neri, J. Ruiz, and F. Martinez Vidal. Search for new physics via baryon EDM at LHC. 2020.

[22] M. E. Pospelov and I. B. Khriplovich. Electric dipole moment of the W boson and the electron in the Kobayashi-Maskawa model. *Sov. J. Nucl. Phys.*, 53:638–640, 1991.

[23] I. B. Khriplovich. Quark electric dipole moment and induced θ term in the Kobayashi-Maskawa model. *Phys. Lett. B*, 173:193–196, 1986.

[24] I. B. Khriplovich and A. R. Zhitnitsky. What is the value of the neutron electric dipole moment in the Kobayashi-Maskawa model? *Phys. Lett. B*, 109:490–492, 1982.

[25] F. J. Botella, L. M. Garcia Martin, D. Marangotto, F. Martinez Vidal, A. Merli, N. Neri, A. Oyanguren, and J. Ruiz Vidal. On the search for the electric dipole moment of strange and charm baryons at LHC. *The European Physical Journal C*, 77(3), Mar 2017.

[26] J. M. Pendlebury et al. Revised experimental upper limit on the electric dipole moment of the neutron. *Phys. Rev. D*, 92:092003, Nov 2015.

[27] G. Aad et al. (ATLAS Collaboration). Measurement of the parity-violating asymmetry parameter α_b and the helicity amplitudes for the decay $\Lambda_b^0 \to J/\psi\Lambda^0$ with the ATLAS detector. *Phys. Rev. D*, 89:092009, May 2014.

[28] E. Leader. *Spin in Particle Physics*. Cambridge University Press, 2001.

[29] R. Aaij et al. (LHCb Collaboration). LHCb detector performance. *International Journal of Modern Physics A*, 30(07):1530022, Mar 2015.

[30] E. Bos and E. Rodrigues. The LHCb track extrapolator tools. Technical report, CERN, Geneva, Nov 2007.

[31] *Runge-Kutta and Extrapolation Methods*, pages 129–353. Springer Berlin Heidelberg, Berlin, Heidelberg, 1993.

[32] Wouter D. Hulsbergen. Decay chain fitting with a Kalman filter. *Nucl. Instrum. Meth. A*, 552:566–575, 2005.

[33] P. Li, E. Rodrigues, and S. Stahl. Tracking definitions and conventions for Run 3 and beyond. Technical report, CERN, Geneva, Feb 2021.

[34] Barbosa-Marinho, P. R. et al. (LHCb Collaboration). LHCb inner tracker: Technical Design Report. Technical report, CERN, Geneva, 2002.